Journal of Applied Physics

REVIEW ARTICLE | JULY 09 2025

Corrosion and oxidation behavior of high entropy alloys in extreme and harsh environments: A perspective on steam corrosion

Amal Sasi ; R. J. Vikram ; K. Dash

J. Appl. Phys. 138, 020701 (2025)
https://doi.org/10.1063/5.0273671

AIP Publishing

Journal of Applied Physics REVIEW pubs.aip.org/aip/jap

Corrosion and oxidation behavior of high entropy alloys in extreme and harsh environments: A perspective on steam corrosion

Cite as: J. Appl. Phys. 138, 020701 (2025); doi: 10.1063/5.0273671
Submitted: 1 April 2025 · Accepted: 14 June 2025 ·
Published Online: 9 July 2025

Amal Sasi,[1] R. J. Vikram,[2] and K. Dash[3,a)]

AFFILIATIONS

[1]Department of Physics, Amrita School of Engineering, Amrita Vishwa Vidyapeetham, Chennai, India
[2]Institute for Applied Materials (IAM-WK), Karlsruhe Institute of Technology (KIT), Engelbert-Arnold-Str. 4, Karlsruhe 76131, Germany
[3]Department of Chemistry, Amrita School of Engineering, Amrita Vishwa Vidyapeetham, Chennai, India

[a)]**Author to whom correspondence should be addressed:** d_khushbu@ch.amrita.edu

ABSTRACT

High-Entropy Alloys (HEAs) have emerged as a novel class of materials exhibiting excellent mechanical, thermal, and corrosion-resistant properties. This paper discusses the application of HEAs in high-temperature steam environments, focusing on their potential as advanced materials for components in geothermal systems, nuclear power plants, and hydrogen fuel cells. These applications demand materials that can withstand harsh conditions, including elevated temperatures, aggressive fluids, and corrosive environments. With their unique composition of multiple elements in equimolar or near-equimolar ratios, HEAs present an intriguing prospect for addressing these challenges. The review summarizes recent research findings on the performance of HEAs in harsh conditions, highlighting their corrosion resistance. The versatility of HEAs, coupled with ongoing advancements in alloy design and processing techniques, opens new avenues for optimizing these alloys for enhanced durability and efficiency. A perspective on the current state of research and future prospects on the above has been discussed here. It sets the stage for further exploration of HEAs as promising candidates for sustainable and resistant materials in aggressive environment applications.

I. INTRODUCTION

The research and development of corrosion-resistant alloys, particularly for steam environments, are of high importance for the efficiency and longevity of power generation systems. In the context of ultra-supercritical power plants, which aim for higher efficiency and lower emission, the study of steam oxidation in advanced alloys is crucial.[1] Research based on Ni-based alloys, such as Inconel 617, Haynes 230, and Haynes 282, as well as high-alloyed steels, has shown promising results in improving steam corrosion resistance.[2,3] The formation of thin and adherent Cr_2O_3 oxides on these alloys can significantly extend the lifetime of superheaters and reheaters in power plant systems.[4] Furthermore, understanding the internal oxidation process [which can lead to accelerated degradation in gamma-prime (γ') strengthened alloys] is essential for optimizing the performance and durability of these alloys.[5,6] Earlier research, i.e., the year 1994 study shown in Fig. 1, primarily focused on the corrosion resistance of alloys under various steam conditions, evaluating the effect of element additions, surface pretreatment, and chemical environments on corrosion behaviors.[2] This research contributed to developing materials with improved corrosion resistance, such as alloys with higher chromium (Cr) content that form protective oxide layers.[3] Recent research, e.g., 2020 and 2022 year studies, has expanded to include corrosion control measures in nuclear steam generators and focuses on sustainable energy systems. These studies highlight the importance of corrosion resistance for the development of climate-resilient energy systems and infrastructure.[7,8]

Investigations on high-entropy alloys (HEAs) in geothermal steam environments face a dearth in the literature. There is

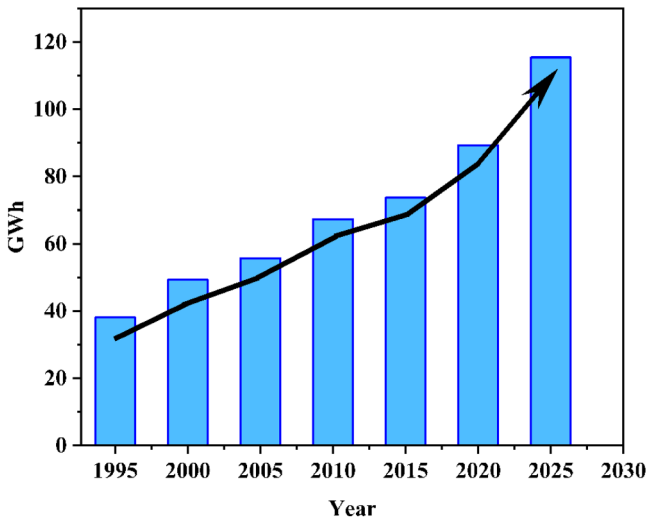

FIG. 1. Worldwide geothermal electricity generation in different years.

insufficient data on their long-term behavior, as most studies focus on mechanical properties or initial corrosion resistance rather than extended evaluations. Additionally, systematic and diverse testing of different HEA compositions under varying geothermal conditions is required to understand their performance and durability better. Geothermal energy is a promising renewable energy source, and its utilization has been increasing in the world in recent years,[9–11] as shown in Fig. 1. In geothermal power production, the machinery in plants and wells is exposed to geothermal steam and water. Corrosive species such as hydrogen sulfide (H_2S), carbon dioxide (CO_2), and chloride ions (Cl^-) are commonly present in geothermal steam.[12] Figure 2 shows the geothermal power system highlighting the corrosive steam generation in the process. The materials in direct contact with steam can experience uniform and localized corrosion.[13] Corrosion problems encountered in the plant can lead to expensive repairs and loss of production.[14] This can be solved with appropriate materials' selection, which are commercially available and good engineering design and practice.[15] Large challenges that need attention include corrosion and erosion problems in turbines, corrosion in high-temperature geothermal well fluid, and deep-drilled superheated geothermal wells.

HEAs face several challenges in geothermal steam environments, including susceptibility to corrosion from chemicals like H_2S and CO_2. Limited understanding of their long-term stability under these extreme conditions has directed investigations to be conducted in laboratories. With minimal real-world testing, it is difficult to predict practical performance. Customizing HEAs for geothermal applications involves high cost and time-consuming trial and error processes. Additionally, HEAs must withstand fluctuating mechanical and thermal cycles, which require optimum combination of mechanical strength and thermal stability. Addressing these issues demands focused research, enhanced testing, and interdisciplinary collaboration, which creates demand to develop new HEAs or engineer existing HEAs to combat high temperatures and pressure wherein corrosive and erosive conditions exist.[16] Conventional alloys like Inconel-617, Haynes-230, and Haynes-282 absorb hydrogen, leading to hydrogen embrittlement. These alloys also undergo degradation and environmental cracking [stress corrosion cracking (SCC) or hydrogen-induced cracking (HIC)], which can affect their performance over time. HEAs have been proposed to be used in harsh environments; for instance, components such as wellbore casings, downhole tools, and heat exchangers. The versatility in alloy design allows tailoring compositions for compatibility with specific geothermal fluid compositions.[17] When compared to conventional materials, HEAs show better performance.[18–20] Higher configurational entropy, similar metallic element character, and mixing enthalpy combinations that favor the formation of solid solutions, such as BCC or FCC over intermetallic compounds, result in solid solution phase stabilization at high temperatures. These characteristics of HEAs are promoted by the combined interactions among all of the fundamental constituents, referred to as "cocktail effect." HEAs have been shown to outperform conventional alloys in terms of wear resistance, oxidation, and corrosion resistance, as well as mechanical properties.[17,21] The number of publications in the field of HEAs has also increased rapidly starting from the year 2015.[22,23] Despite numerous recent studies on the corrosion behavior of HEAs, certain aspects remain unclear. Investigation of the stability of the passive film and its correlation with the alloy composition is of significance to the materials' community. The phenomenon of passivation is a common feature of HEAs, resulting from incorporating passivating elements like Hf, Ti, Cr, Ni, Fe, and Al. Each of these elements reacts with corrosive species and forms respective oxides on the surface and prevents further corrosion. The alloy structure and the composition of the passive film lead to distinct electrochemical response. The nature of these responses depends on the type and content of alloying elements. This discussion correlates the intricate relationship between corrosion resistance, the stability of passive films, and alloy composition in HEAs. Various aspects of the influencing factors of corrosion in HEAs have been elaborated and delibrated. Overall, HEAs play an important role in improving the integrity and performance of components in geothermal applications, supporting the growth of this renewable and environment friendly energy source.

II. STATE-OF-THE-ART

A. Geothermal steam corrosion

Geothermal energy is a renewable and sustainable source of power that harnesses the earth's natural heat. The process involves extracting high-temperature steam from beneath the earth's surface to generate electricity. While geothermal power generation systems possess immense potential, the chemical composition of geothermal steam poses significant challenges to the durability and efficiency of the materials used in power plants. Geothermal steam contains water vapor (H_2O) mixed with gases such as hydrogen sulfide (H_2S), carbon dioxide (CO_2), methane (CH_4), nitrogen (N_2), hydrogen (H_2), and oxygen (O_2), as well as dissolved ions like chloride (Cl^-), sodium (Na^+), and calcium (Ca^{++}). These chemical species are highly corrosive and can severely degrade metal and

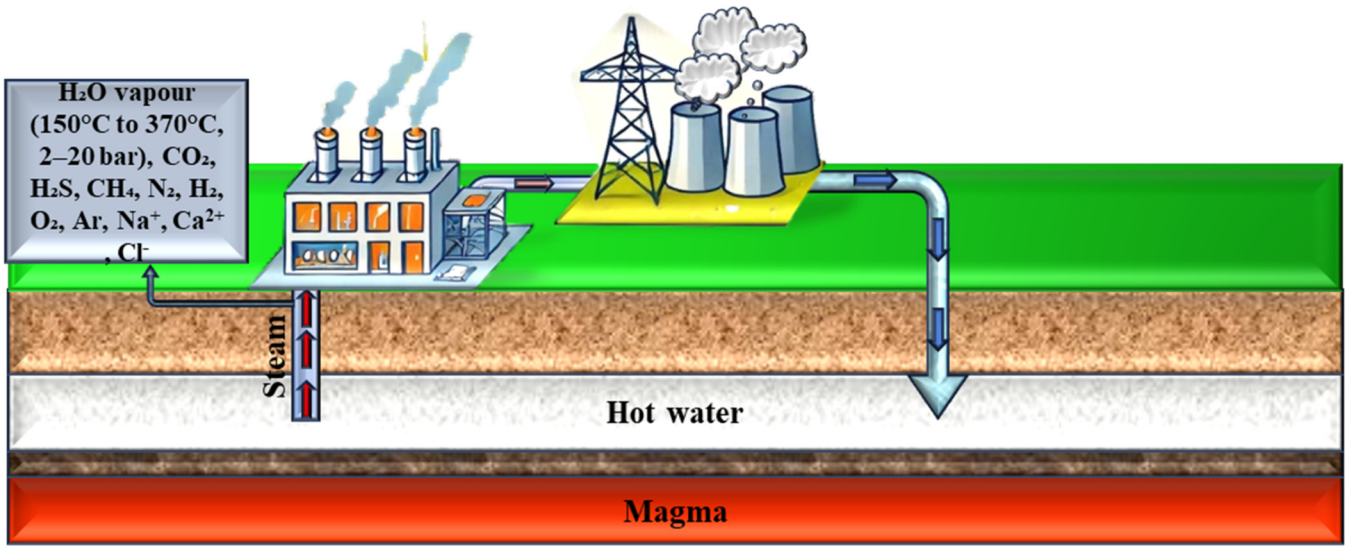

FIG. 2. Geothermal power system highlighting corrosive steam that impacts plant durability (parts of this figure were drawn using Microsoft Designer).

alloy components, leading to high maintenance and reduced efficiency. Hydrogen sulfide (H_2S), carbon dioxide (CO_2), and chloride ions (Cl^-) are key contributors to material degradation due to their aggressive corrosive properties. H_2S is highly corrosive, causing severe pitting and embrittlement of metals, while CO_2 reacts with water to form carbonic acid, creating acidic environments that accelerate corrosion. Chloride ions further intensify localized corrosion mechanisms like pitting and crevice corrosion. Environmental factors such as high temperatures, pressures, and mixed gases exacerbate these effects, significantly increasing the rate and severity of material degradation. Understanding the stages of corrosion in geothermal systems is critical for designing effective mitigation strategies and ensuring the longevity and efficiency of the infrastructure. Sections II A 1 a–II A 1 e outline the key stages of corrosion in geothermal systems from initial steam exposure to the eventual degradation of materials. Figure 3 illustrates the stages of corrosion in geothermal systems, from initial steam exposure to eventual degradation of the metal surface.

1. Stages of corrosion in geothermal systems

a. Steam exposure. The initial stage of corrosion begins with the interaction between geothermal steam and metal surfaces. Components such as pipelines, turbines, and heat exchangers are exposed to steam at temperatures ranging from 150 to 370 °C and pressures of 2–20 bar. The steam's reactive gases, such as H_2S and CO_2, along with chloride ions (Cl^-), initiate chemical reactions upon contact with the metal surface. This interaction disrupts the stability of the metal, creating conditions conducive to corrosion.

b. Corrosion reaction. In this stage, electrochemical reactions occur on the metal surface. Species like H_2S, Cl^-, and hydroxide ions (OH^-) attack the metal, leading to electron transfer and the formation of metal ions. These reactions create localized anodic and cathodic regions on the surface, which accelerate the corrosion process. This localized deterioration is often manifested as pitting, wherein small, deep holes form on the metal surface.

c. Formation of oxide layer. As a by-product of corrosion, an oxide layer forms on the metal surface. Initially, this layer acts as a protective barrier, slowing the rate of further corrosion. However, in geothermal environments, the oxide layer becomes porous and brittle due to the presence of ions like Cl^- and H_2S. This instability allows the corrosion process to persist, compromising the layer's protective properties.

d. Ion diffusion. The next stage involves the penetration of ions through the oxide layer. Chloride ions (Cl^-) diffuse through the porous oxide, reaching the underlying metal. This leads to accelerated electrochemical reactions, where the accumulation of corrosion products weakens the oxide layer further. The metal surface develops distinct anodic and cathodic regions, promoting localized corrosion.

e. Degradation. Over time, the passive oxide layer cracks and detaches, exposing the base metal to further attack. This results in the formation of rust, surface cracks, and significant material loss. Continuous degradation weakens the structural integrity of components, leading to failures in pipelines, heat exchangers, and turbines. Such failures can cause leaks, reduce efficiency, and even result in system shutdowns.

B. Impact of geothermal steam

Uniform corrosion occurs when the surface material experiences even thinning, often caused by acidic or basic fluids in

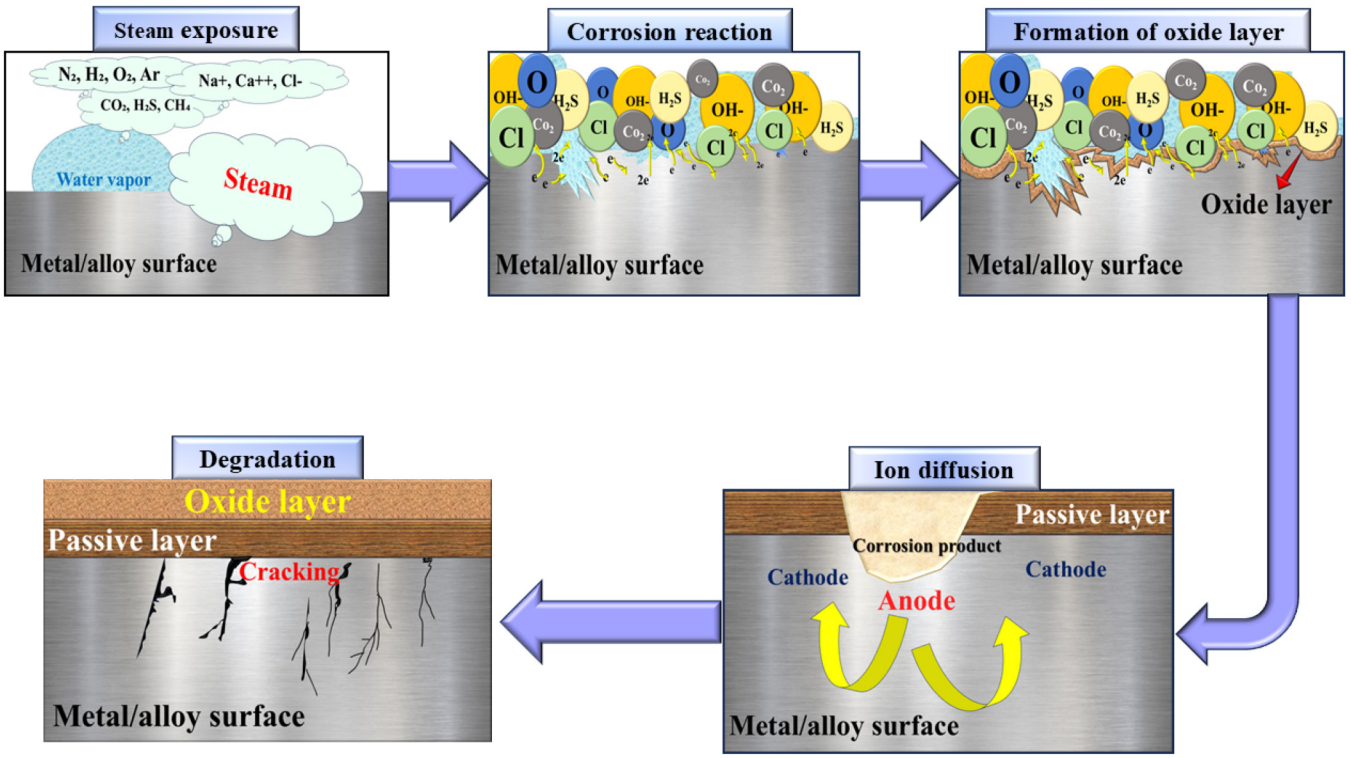

FIG. 3. Stages of corrosion in geothermal systems.

geothermal brines, leading to a gradual loss of strength. Pitting corrosion results in localized pits on the metal surface, promoted by the presence of chloride ions, while crevice corrosion occurs in confined spaces like joints and seals, where stagnant fluid causes accelerated material failure. Galvanic corrosion happens when dissimilar metals are in contact, with one metal deteriorating faster due to the presence of geothermal fluids as an electrolyte. Stress corrosion cracking (SCC) occurs when tensile stress and a corrosive environment combine, often causing catastrophic failures in components exposed to sulfides, chlorides, or carbon dioxide. Erosion–corrosion prevails when high-velocity geothermal fluids carry particles that cause both mechanical wear and chemical attack, rapidly degrading materials, particularly in pipelines and pumps. Hydrogen embrittlement weakens metals exposed to hydrogen sulfide (H_2S), leading to brittle fractures, while sulfide stress corrosion cracking (SSCC) results from hydrogen sulfide interacting with high-strength steels, leading to sudden failures. Carbon dioxide corrosion (sweet corrosion) occurs when dissolved CO_2 reacts with water to form carbonic acid, which degrades carbon steels. Finally, microbiologically influenced corrosion (MIC) is caused or accelerated by microorganisms such as sulfate-reducing bacteria (SRB) producing hydrogen sulfide and forming biofilms, which lead to localized damage and pitting. These various forms of corrosion can significantly impact the efficiency, reliability, and lifespan of geothermal systems. Figure 4 showing geothermal steam's corrosive nature leads to various types of corrosion in power plants.

C. Impact of geothermal corrosion

Economically, the costs of replacing corroded parts and repairing infrastructure are high, especially with the need for specialized corrosion-resistant materials. These expenses are compounded by reduced efficiency, leading to higher energy losses and lower output, which can also result in revenue losses due to prolonged downtime. Environmentally, corrosion poses significant risks, such as leaks of geothermal fluids containing harmful substances like hydrogen sulfide (H_2S) and heavy metals. These leaks can lead to soil, groundwater, and surface water contamination, disrupting local ecosystems. Furthermore, the release of toxic gases like H_2S due to corrosion threatens both workers and nearby communities. The safety concerns associated with corrosion include sudden equipment failures that could lead to accidents or blowouts, posing risks to both personnel and infrastructure. Finally, corrosion accelerates the wear and tear of components, significantly reducing their lifespan and undermining the overall reliability of geothermal systems, causing frequent interruptions in energy generation. These combined impacts necessitate the need for effective corrosion management to ensure the longevity and efficiency of geothermal energy production.

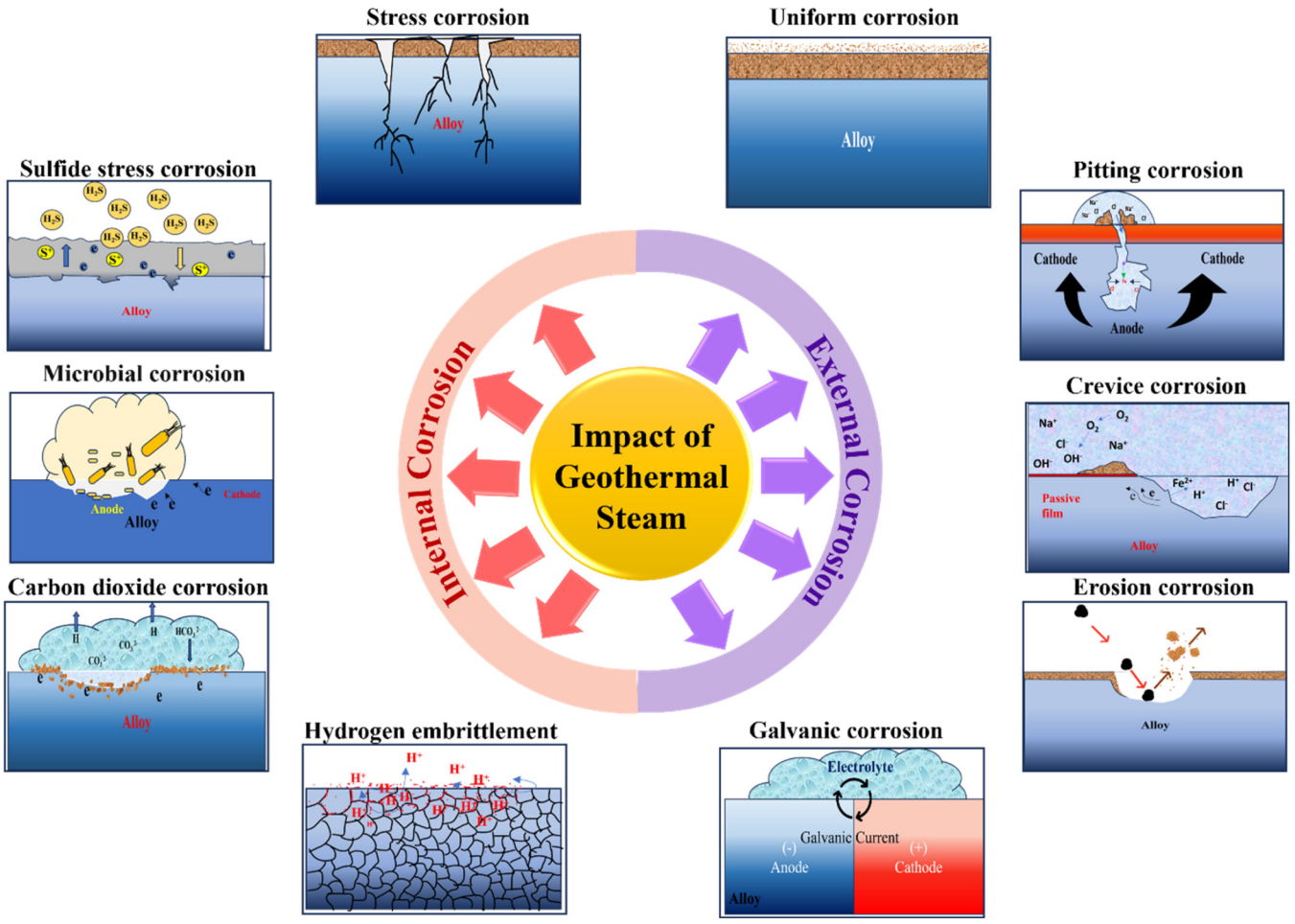

FIG. 4. Corrosive nature of geothermal steam resulting in different types of corrosion in power plants.

D. Cost of corrosion

The effects of corrosion span our daily life by both direct and indirect means. Corrosion is considered one of the significant problems for most of the industrialized countries.[24] When designing any machinery for industry, the effect of corrosion on the equipment and its surroundings always deserves to be a significant cost incurring issue. Oil companies all over the world spend huge amount of money to manage the corrosion problem.[25] Nevertheless, disasters such as casualties, economic losses, and environmental side effects triggered by corrosion still happen quite often. The maintenance cost of corrosion-related issues for a particular country varies from 1% to 5% of its gross national product (GNP).[9] NACE International conducted a global study on corrosion costs and preventative strategies in 2013, which was utilized in the World Bank economic sector and global Gross Domestic Product (GDP) data to relate the cost of corrosion. This study showed that the estimated global cost of corrosion was approximately 3.4% of the GDP and the cost of corrosion in Gulf Cooperation Council (GCC) countries[26] (Fig. 5).

E. Corrosion challenges in power generation plants and potential solutions

Structural materials in many front-line high-technology areas must operate under extreme conditions of temperature, pressure, and corrosive environments.[27] So, material degradation at high temperatures is a serious problem in several high-tech industries. Gas turbines in aircraft, fossil-fueled power plants, refineries, petrochemical industries, and heating elements for high-temperature furnaces are some examples where corrosion limits their use or reduces their life, considerably affecting their efficiency.[28] The existing preventive methods of steam corrosion and erosion in aggressive environments are (a) alloying additions, (b) use of inhibitors, and (c) coatings.[29] The majority of corrosion resistance efforts have been concentrated on a variety of steels and nickel alloys, such as

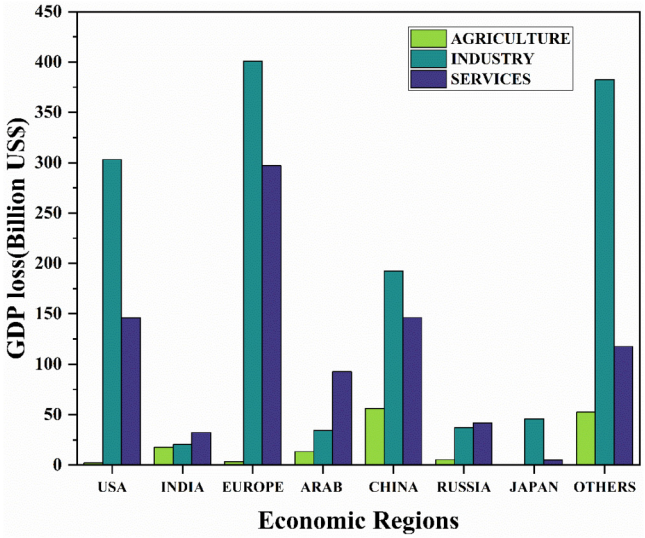

FIG. 5. GDP loss due to corrosion costs of different countries.

IN 617, Alloy 800, Alloy 600, Alloy 690, and IN 718.[30–32] An effective solution to the above corrosion-prone alloys could be HEA coatings, which offer several benefits, such as enhancing their resistance to steam corrosion.[16] HEA coatings impede stress corrosion cracking, oxidation, fatigue, and parabolic growth rates, which reduce the corrosion rate of nickel-based alloys in high-temperature steam environments.[33] This performance offers superior strength and corrosion resistance suitable for applications in gas turbines, power generation, and petrochemical plants where these alloys are commonly utilized. HEA coatings offer economic advantages over the component lifecycle by reducing maintenance requirements, extending service intervals, and improving operational reliability in steam corrosion environments.

III. RESEARCH FINDINGS

A. Effect of phases on steam corrosion behavior of HEAs

HEAs typically exhibit either body-centered cubic, face-centered cubic, or a blend of these two phases.[22] Materials with a stable crystal structure can form protective oxide layers that shield them from further degradation, thereby enhancing their durability in harsh environments. $Al_{x(x=0.2,\ 0.4,\ 0.6)}CrCuFeNi_2$[34] promotes the formation of protective Al_2O_3 and Cr_2O_3 oxide scales while reducing the formation of Fe-rich oxides, resulting in improved oxidation resistance and the development of thinner, more stable oxide layers. Cr in the $Mo_{0.5}VNbTiCr_{x(x=0\text{–}2.0)}$[35] alloy promotes the formation of the Laves phase and leads to a more complex multiphase microstructure that is hard and consists of dense intermetallic compounds (e.g., C15-type) along grain boundaries. This acts as a physical barrier to oxygen and other corrosive species, slowing down diffusion into the matrix and improving corrosion resistance at high temperatures. Adding "Mn" to the AlCrFeNi matrix results in a mixed-phase (FCC–BCC). However, when "Mn" is replaced with Cr, it results in a single-phase alloy (FCC).[19] The steam corrosion-resistant alloys include 45.2% of HEAs that are FCC, 35.5% are BCC, and 19.4% are a combination of these phases (which includes 80.7% single-phase HEAs and 19.4% multi-phase HEAs). Notably, alloys with FCC and combined FCC + BCC structures demonstrate superior resistance to high-temperature steam corrosion compared to those with BCC structures.[36–40]

B. Influence of microstructure on corrosion performance of HEAs

Understanding the microstructure of HEAs serves as a blueprint to predict the corrosion performance. Grain boundaries within HEAs can serve as preferential sites for corrosion initiation, influenced by factors such as elemental segregation and structural defects. Moreover, the presence of precipitates and second phase alters local chemical compositions, thereby impacting the formation and stability of protective oxide layers. The microstructure also affects diffusion pathways for corrosive agents like steam and oxygen, influencing the kinetics of oxide formation and corrosion processes. Furthermore, surface morphology that is implication of roughness and grain size, which plays a role in the adhesion and stability of oxide scales, ultimately affecting the overall corrosion behavior of HEAs.[37,41]

Chromium addition to HEAs can significantly improve their corrosion resistance by promoting the formation of protective oxide layers, stabilizing simple solid solution phases, and synergistically interacting with other alloying elements like Al. $Mo_{0.5}VNbTiCr_{x(x=0,\ 0.25,\ 0.5,\ 0.75,\ 1.0,\ 1.5,\ 2.0)}$[35] demonstrates a significant correlation between corrosion, with the addition of Cr. As the Cr content in the HEAs increases beyond a concentration of 1.0, the formation of the Laves phase begins, resulting in enhanced corrosion resistance against severe conditions (superheated steam at 400 °C and 10.3 MPa for 1680 h), exhibiting the least mass gain. Similarly, $Al_xCrCuFeNi_{2(x=0.2,\ 0.4,\ 0.6)}$[34] HEAs follow the same trend with increasing concentration of Al. High Mo concentration in the (Mo, Cr) rich phase forms FCC solid solution of the CoCrFeNiMo alloy. This reduces the Cr concentration in the other phases (Mo rich phases and Ni–Fe-rich phases), resulting in lower corrosion resistance.[42]

The as-cast FeNiCrCuAl[43] HEAs possesses NiAl-rich BCC (B2) phase surrounding the FeCr-rich region petal-like microstructure contributing to lower mass gains. This is notably less than those of austenitic stainless steels and Ni-based alloys under identical corrosion conditions (1000 h at 550 °C and 25 MPa). In a similar family of alloys of AlCrFeNiMn[44] where Mn replaces Cu, characteristic dendritic segregation (DR) pattern is observed. As the heat treatment temperature rises, the precipitation of the BCC phase is enhanced, transforming microscale needle-like structures into nanoscale granular structures. Treatment at 800 °C results in the dispersion of ultrafine precipitates, reducing the coarse DR. Further heating (900 °C) leads to a decrease in ultrafine precipitates and a weakening of the DR structure. Simultaneously, at 1000 °C, the second phase becomes passivated, with the emergence of a twin. This dendritic segregation in the HEA leads to active corrosion and dissolution of the alloy, as indicated by a high corrosion

rate of 3.25 mm/year. On the other hand, in the $Al_{6.5}Cr_{21.3}Fe_{22.9}Ni_{24.1}Co_{24.1}$ matrix, the addition of reactive elements (Zr or Y) leads to segregation at dendritic domain boundaries, limiting coalescence, which results in grain refinement showing slight variation in corrosion resistance. However, $Al_{7.9}Cr_{23.2}Ni_{34.8}$ consists of a single FCC solid solution, while $Al_{8.9}Cr_{23.1}Ni_{34.3}$ has FCC plus B2–NiAl phases, but the addition of Nb or Ti promotes the formation of the Laves phase (Fe_2Nb) and γ'-$Ni_3(Al, Ti)$ within the FCC solid solution matrix and this contributed to an increase in weight gain compared to $Al_{7.9}Cr_{23.2}Ni_{34.8}$ and $Al_{8.9}Cr_{23.1}Ni_{34.3}$. Figure 6 shows the surface morphologies of oxides formed on FeNiCrCuAl after exposure to supercritical water (SCW) at various temperatures (380, 500, and 650 °C) and durations (100–500 h). The images reveal temperature- and time-dependent evolution of oxide microstructural features like striped (Al_2O_3), polyhedral [$FeCr_2O_4$ and $(Al,Fe)_3O_4$], and flakes (Cu_2O), indicating the changes in oxidation mechanisms and scale stability. Cu_2O particles are rough and become less dense over time at 380 °C [Figs. 6(a)–6(c)], whereas polyhedral $FeCrO_4$ and Al_2O_3 stripes form in NiAl- and FeCr-rich regions, respectively. The $FeCrO_4$ content increases over time at a particular temperature. Both Cu_2O and $FeCr_2O_4$ particles enlarge at 500 °C [Figs. 6(d)–6(f)], with flaky Al_2O_3 and Cu_2O predominating in NiAl-rich regions and $FeCr_2O_4$ covering FeCr-rich zones. This indicates enhanced oxide segregation at higher temperatures. While smaller Cu_2O particles continue to exist, flaky Al_2O_3 becomes the predominant phase on NiAl regions at 650 °C [Figs. 6(g)–6(i)]. At the same time, a synchronous Cr/Al-rich oxide film forms on FeCr regions, Al_2O_3-based protection becoming predominant at higher temperatures (Table I).[45]

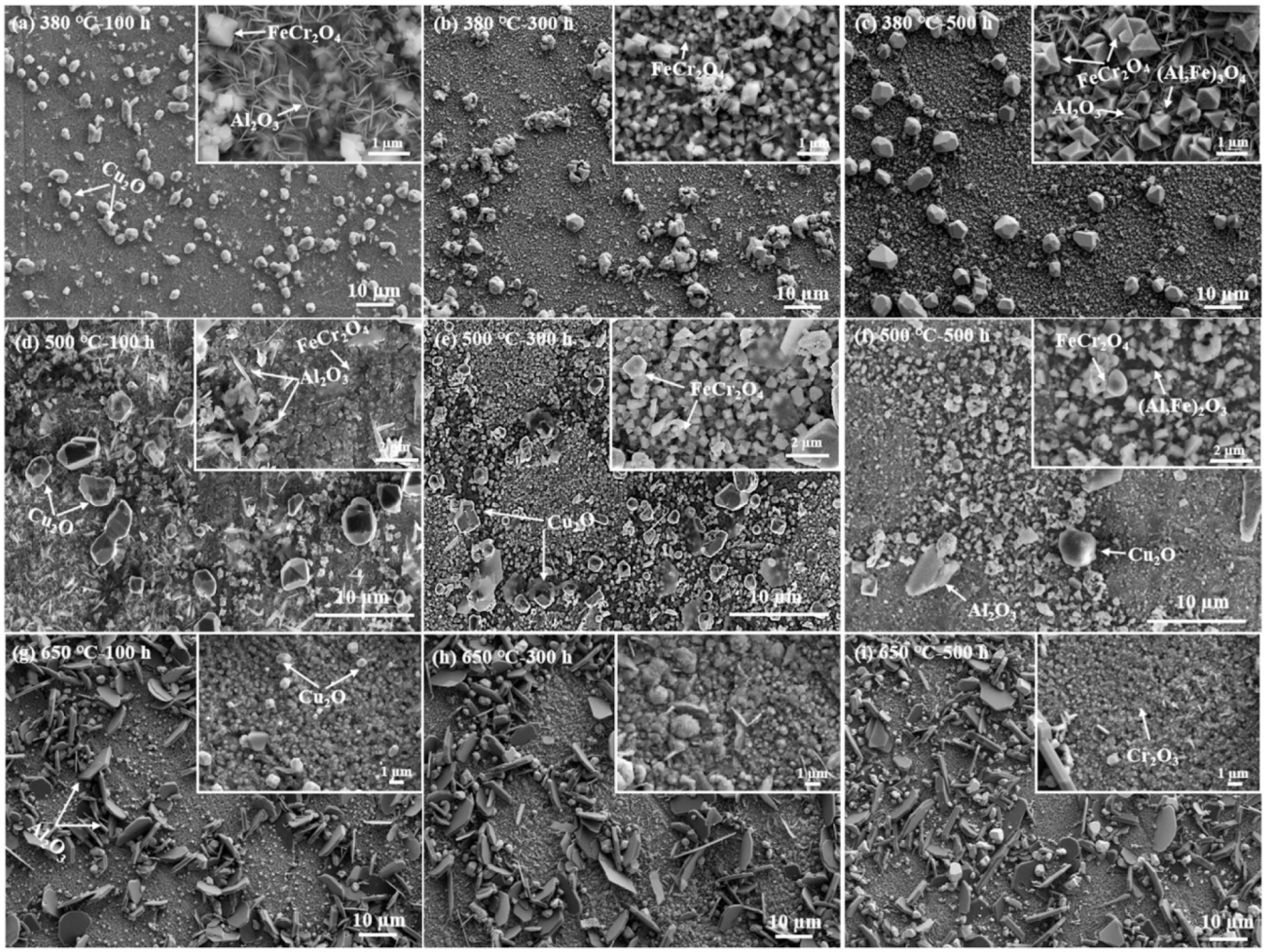

FIG. 6. Surface morphologies of the oxides developed on FeNiCrCuAl after exposure to SCW for different exposure times at different temperatures.[45] Reproduced with permission from Zhao *et al.*, Corros. Sci. **227**, 1–15 (2024). Copyright 2024 Elsevier.

TABLE I. High-entropy alloys and their crystal structure.

S. No.	Alloy	Crystal structure	Reference
1	$Al_{7.9}Cr_{23.2}Fe_{34.1}Ni_{34.8}$	Austenite	46
	$Al_{8.9}Cr_{23.1}Fe_{33.7}Ni_{34.3}$	Austenite	
	$Al_{8.2}Cr_{21.4}Fe_{30.3}Ni_{35}Nb_{5.1}$	Fe_2 Nb (laves)	
	$Al_{7.9}Cr_{22}Fe_{31.9}Ni_{33.2}Ti_5$	Austenite + Ni_3 (Al,Ti)	
2	$Al_{11.1}Cr_{22.2}Fe_{22.2}Ni_{22.3}Mn_{22.2}$	FCC + BCC + B2	41
	$Al_{13.0}Cr_{21.7}Fe_{21.7}N_{21.8}Co_{21.7}$	FCC + BCC + B2	
	$Al_{12.7}Cr_{21.6}Fe_{21.7}Ni_{21.7}Co_{21.6}Zr_{0.06}$	FCC	
	$Al_{12.7}Cr_{21.6}Fe_{21.7}Ni_{21.7}Co_{21.6}Y_{0.06}$	FCC + BCC	
3	AlCrNbTiZr	BCC	47
4	FeCrMnNi	BCC + FCC	48
5	FeNiCrCuAl	BCC + FCC	49
6	AlCrNbSiTi		50
7	$(FeNi)_{67}Cr_{15}Mn_{10}A_{l5}Ti_3$	FCC + BCC	36
8	CoCrFeNiMo	Fe_3Ni_2 (laves) + FCC, Cr, Mo (laves)	41
9	FeCoNiCr	FCC	50
	FeCoNiCrMo	FCC	
	FeCoNiCrTi	BCC + FCC	
	FeCoNiCrMn	FCC	
10	Al_xCrCuFeNi2 ($x = 0.2$, 0.4, and 0.6)	FCC	34
11	AlCrFeNiMn	FCC + BCC	43
12	FeNiCrCuAl	FCC + BCC	42
13	CoCrFeNiMn	FCC	52
14	$Al_{25}Co_{25}Cr_{25}Ni_{25}$	BCC + σ	53
	$Al_{20}Co_{25}Cr_{25}Ni_{25}Si_5$	BCC + σ	
	$Al_{20}Co_5Cr_{20}Fe_{20}Ni_{35}$	BCC + FCC	
	$Al_{10}Co_{15}Cr_{20}Fe_{20}Ni_{35}$	BCC + FCC	

C. Oxidation behavior of HEAs in harsh and hostile environments

Oxidation can be influenced by several factors, including the specific elements present in the alloy, temperature, the environment in which the oxidation occurs, and the presence of impurities or contaminants. Oxidation kinetics aids in understanding the nature of oxide formed in a particular environment. Linear kinetics indicate the formation of a non-protective oxide layer that allows continuous oxygen penetration, resulting in a constant oxidation rate over time. In contrast, parabolic kinetics reflect the development of a dense, protective oxide scale (like Al_2O_3 or Cr_2O_3), where oxidation slows down, as diffusion through the oxide layer becomes rate-limiting. The transition from linear to parabolic behavior often signals improved oxidation resistance in HEAs.[54–56]

An excellent equiatomic composition with superior steam corrosion-resistant behavior would be $Al_{25}Co_{25}Cr_{25}Ni_{25}$.[61] This alloy displays remarkable oxidation resistance in steam environments at 1000 °C, particularly under conditions involving rapid temperature changes, making it well-suited for resisting oxidation challenges in dynamic thermal environments. The weight gain of the FeNiCrCuAl HEA gradually increases with extended exposure periods to supercritical water (SCW), following a parabolic growth law. Identified oxide films on this alloy surface include $FeAl_2O_4$, $NiAl_2O_4$, γ-Al_2O_3, and Cu_2O after 100 h of exposure.[42] The $Al_{0.2}CrCuFeNi_2$ HEA[34] exhibits two-stage oxidation kinetics at 700 °C, with an initial fast-growing stage before 25 h and a slow-growing stage within 100 h. $Al_{0.4}CrCuFeNi_2$ and $Al_{0.6}$ $CrCuFeNi_2$ HEAs show single parabolic rate constants. A lower solute concentration of Al in $Al_{0.2}CrCuFeNi_2$ leads to a discontinuous Al_2O_3 distribution and thicker Fe–Ni-rich spinel oxides. $Al_{0.4}CrCuFeNi_2$ and $Al_{0.6}CrCuFeNi_2$ HEAs exhibit less Cu_2O and NiO oxide and thinner spinel oxide scales. Spinel becomes part of the growing oxide layer on the alloy surface. This layer can act as a partial barrier to further oxidation.[41] At 380 °C, irregular Cu_2O particles, Al_2O_3 striped oxides, and $FeCr_2O_4$/(Al, Fe)$_3O_4$ polyhedral oxide particles develop on NiAl-rich and FeCr-rich regions in CoCrNiFeMo.[41] Duplex/triplex structured oxide films form on NiAl-rich and FeCr-rich regions at 380 °C. At 500 °C, oxide sizes increase, and at 650 °C, flaky Al_2O_3 oxides are larger and denser; this leads to exhibiting strong corrosion resistance.

The $Al_{0.5}CrFeNiMn$ alloy[58] exhibits poor oxidation resistance in air. Oxide scales consist of a thick Mn_3O_4 single layer and a triple-layer assembly (Mn_2AlO_4/$MnAl_2O_4$/Al_2O_3) in steam, indicating reduced oxidation rates in steam. Distinct scaling behaviors are attributed to varying oxygen partial pressures and preferential initial oxidation of Mn. $Al_{0.5}CrFeNiCo$ alloys exhibit selective oxidation of Al, forming a dense and protective alumina scale, showcasing excellent high-temperature oxidation resistance comparable

to alumina-forming FeCrAl alloys. However, the oxide scales show low adherence with significant peeling off during cooling.

HEAs with $Al_{(7.9–8.9)}Cr_{(21.4–23.2)}Ni_{(34.3–35)}$[46] forms α-$Al_2O_3$ scales during exposure to steam at 1200 °C. Adding Nb improves oxide scale adherence, while adding Ti degrades oxidation resistance due to the formation of less protective TiO_2 and Fe_3O_4 layers. The oxygen dissociation partial pressures of metal oxides such as Al_2O_3, TiO_2, Nb_2O_5, Cr_2O_3, and Fe_3O_4 are lower than the oxygen partial pressure of steam (0.5 bar) at 900–1300 °C. This shows their thermodynamic stability in a steam atmosphere.[62]

D. Comparison of steam corrosion behavior of HEAs with conventional superior alloy

The corrosion layer primarily comprises sulfide- and oxide-rich corrosion products, indicating aggressive reactions with H_2S and CO_2 gas in geothermal steam. $CoCrNiFeMo_{0.5}$ is the most corrosion-resistant among CoCrNiFeMo alloys. Corrosion rates of Cu-containing HEAs (CoCrNiFeMoCu) increase with higher Cu concentrations in a simulated superheated geothermal environment, with the main corrosion product identified as Cu_2S. The reaction between H_2S and Cu is responsible for the corrosion process.[41]

Both $(FeNi)_{67}Cr_{15}Mn_{10}Al_5Ti_3$ and Zr-4 alloys gain weight in a 360 and 400 °C high-temperature and high-pressure steam environment, with HEA exhibiting lower weight gain compared to the Zr alloy over a time period of 336 h. The HEA's weight gain is significantly lower than that of the conventional Zr alloy as time progresses. Steam vapor corrosion resistance varies significantly with bias voltage, where samples with a 50 V bias exhibit corrosion pits between 140 and 200 h, while other conventional alloys show pits between 50 and 140 h.[66]

The FeCrMnNi alloy experiences weight loss in a 360 °C high-temperature and high-pressure water environment, with evenly distributed oxide particles formed on the surface, mainly consisting of Fe and Cr oxides, whereas weight gain occurs at 400 °C, indicating poor corrosion performance compared to the former. Oxide particle size is smaller at 400 °C, suggesting a difference in corrosion behavior between the two environments. This HEA has superior steam corrosion resistance compared to other HEAs. Various Fe compositions had been tested for steam corrosion performance under high temperatures (380–1200 °C) at different time scales (1–1680 h), and the results showed an outstanding corrosion resistance. In the case of mass gain, it ranges from 0.00268 mg/cm^2 for FeNiCrCuAl[43] to 0.2 mg/cm^2 for FeCoNiCrMn.[41] Coatings, regardless of deposition temperature, exhibit good hydrophobicity. After 45 days of high-temperature corrosion, all coatings exhibit good corrosion performance, with RT-deposited coatings showing superior high-temperature corrosion resistance. Conventional model alloy (FeAlCrNi) from both alumina-forming austenitic (AFA) and HEA systems exhibits similar corrosion behavior, forming protective alumina scales with comparable thickness, except for HEA with Ti. Al and Cr are the most used elements in steam corrosion-resistant HEAs. Cr does not provide any direct protection against steam corrosion unlike Al, but it gives a phase stability in HEAs that leads to less mass gain under such extreme conditions. HEAs and traditional alloys differ significantly in their steam corrosion

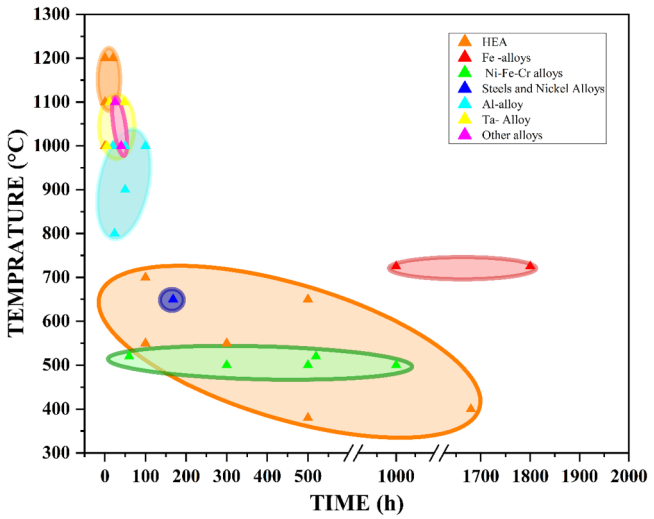

FIG. 7. Ashby plot showing various alloys under steam corrosion conditions.

properties.[21] Conventional alloys, such as Fe, Al, and nickel-based alloys, are widely used in high-temperature corrosive environments. These alloys typically contain a primary element along with smaller amounts of other alloying additions to enhance specific properties. Figure 7 shows the comparison of various alloys of corrosion resistance under harsh environments. Examining Fe-alloys at a temperature of 750 °C over a period of 1000–1800 h revealed a mass gain within the range of 0.15–1.5 mg/cm^2.[67] Conversely, Al-alloys, Ta-alloys, and other alloys subjected to steam corrosion at temperatures between 800 and 1100 °C for a period of less than 100 h displayed mass gain ranging from 9 to 220, 0.9 to 22, and 8 to 18 mg/cm^2, respectively. Steels and nickel alloys exhibited a mass gain of 0.1–6.63 mg/cm^2 under the conditions of 600 °C for 150 h. Notably, Ni–Fe–Cr alloy experienced mass loss, indicating vulnerability to steam corrosion, necessitating regular replacement.

In contrast, HEAs demonstrated exceptional resistance to steam corrosion, with compositions tailored for both high temperatures (1100–1200 °C) over short durations (<100 h) and low temperatures (400–700 °C) spanning longer periods (100–1700 h). HEAs exhibited mass gains of 0.025–19.4 and 0.0268–15.2 mg/cm^2 under these respective conditions. Consequently, HEAs emerge as highly significant in mitigating steam corrosion, rendering them suitable for applications in supercritical steam environments (Table II).

E. HEA coatings as a plausible solution for steam corrosion

High-entropy alloy coatings are healthy alternatives for anti-steam corrosion applications due to their superior corrosion resistance, thermal stability, and mechanical strength. HEAs as bulk materials are expensive because they require several rare or expensive elements. Coating them as thin coatings onto inexpensive substrates has both practical and financial benefits.[85–87] This targeted

TABLE II. Mass gain of HEAs at various conditions.

	Composition	Time (h)	Temperature (°C)	Mass gain (mg/cm^2)	Reference
HEA	CoCrFeNiMn	100	1000	1.75	57
	FeNiCrCuAl	100	550	0.14	42
	$Al_{0.2}CrCuFeNi_2$	100	700	0.17	34
	$Al_{0.4}CrCuFeNi_2$	100	700	0.075	
	$Al_{0.6}CrCuFeNi_2$	100	700	0.025	
	FeCoNiCr	300	550	0.07	50
	FeCoNiCrMo	300	550	0.04	
	FeCoNiCrTi	300	550	0.07	
	FeCoNiCrMn	300	550	0.2	
	$Mo_{0.5}VNbTiCr_x$ (x = 0)	1680	400	12.18	35
	$Mo_{0.5}VNbTiCr_x$ (x = 0.25)	1680	400	12.46	
	$Mo_{0.5}VNbTiCr_x$ (x = 0.5)	1680	400	15.2	
	$Mo_{0.5}VNbTiCr_x$ (x = 0.75)	1680	400	10.84	
	$Mo_{0.5}VNbTiCr_x$ (x = 1.0)	1680	400	7.64	
	$Mo_{0.5}VNbTiCr_x$ (x = 1.5)	1680	400	9.58	
	$Mo_{0.5}VNbTiCr_x$ (x = 2.0)	1680	400	6.56	
	FeNiCrCuAl	500	380	0.00268	49
	FeNiCrCuAl	500	500	0.0067	
	FeNiCrCuAl	500	650	0.0135	
	AlCrNbTiZr	0.5	1000	6.125	47
	AlCrNbTiZr	0.5	1100	13.251	
	AlCrNbTiZr	0.5	1200	19.414	
	$Al_{11.1}Cr_{22.2}Fe_{22.2}Ni_{22.3}Mn_{22.2}$	20	1000	5.2	41
	$Al_{11.1}Cr_{22.2}Fe_{22.2}Ni_{22.3}Mn_{22.2}$	20	1200	37.1	
	$Al_{13.0}Cr_{21.7}Fe_{21.7}Ni_{21.8}Co_{21.7}$	20	1000	0.1	
	$Al_{13.0}Cr_{21.7}Fe_{21.7}Ni_{21.8}Co_{21.7}$	20	1200	1.5	
	$Al_{12.7}Cr_{21.6}Fe_{21.7}Ni_{21.7}Co_{21.6}Zr_{0.06}$	20	1000	0.5	
	$Al_{12.7}Cr_{21.6}Fe_{21.7}Ni_{21.7}Co_{21.6}Zr_{0.06}$	20	1200	7	
	$Al_{12.7}Cr_{21.6}Fe_{21.7}Ni_{21.7}Co_{21.6}Y_{0.06}$	20	1000	0.1	
	$Al_{12.7}Cr_{21.6}Fe_{21.7}Ni_{21.7}Co_{21.6}Y_{0.06}$	20	1200	2	
	$Al_{7.9}Cr_{23.2}Fe_{34.1}Ni_{34.8}$	1	1200	0.39	45
	$Al_{8.9}Cr\ 23.1\ Fe_{33.7}Ni_{34.3}$	1	1200	0.24	
	$Al_{8.2}Cr_{21.4}Fe_{30.3}Ni_{35}Nb_{5.1}$	1	1200	0.72	
	$Al_{7.9}Cr_{22}Fe_{31.9}Ni_{33.2}Ti_5$	1	1200	2.66	
Steels and nickel alloys	304	168	650	6.63	60
	316	168	650	1.74	
	321	168	650	0.34	
	347	168	650	3.87	
	Inconel 600	168	650	0.22	
	Inconel 625	168	650	0.1	
	Inconel X750	168	650	0.19	
	Incoloy 800	168	650	0.21	
	GE Rene 41	168	650	0.14	
Nb-alloy	$NbCrMo_{0.55}Ta_{0.5}TiZr$	100	1000	120	61
	$NbCrMoTiAl_{0.5}$	20	1300	150	62
	$NbCrMoVAl_{0.5}$	20	1300	350	
	$NbCrMoTiVAl_{0.5}$	20	1300	260	
	$NbCrMoTiVAl_{0.5}Si_{0.3}$	20	1300	185	
	NbMoCrTiAl	48	1100	8	63
	NbMoCrTiAlY	48	1000	25	64
	$Nb_{1.3}Si_{2.4}Ti_{12.4}Al_{3.5}Hf_{0.4}$	100	1200	1.5	65
	NbTiZrCr	100	1000	100	

TABLE II. (*Continued.*)

	Composition	Time (h)	Temperature (°C)	Mass gain (mg/cm^2)	Reference
Al-alloy	$Al_{20}Cr_{10}Mo_{10}Nb_{20}Ti_{20}Zr_{20}$	20	1000	21	66
	$Al_{30}Cr_{10}Nb_{20}Ti_{20}Zr_{20}$	20	1000	20	
	$Al_{10}Cr_{30}Nb_{20}Ti_{20}Zr_{20}$	20	1000	39	
	$AlNbTiVZr_{0.25}$	50	900	220	67
	$Al_{20}Nb_{30}Ta_{10}Ti_{30}Zr_{10}$	100	1000	50	68
	$Al_{20}Cr_{25}Nb_{20}Ti_{20}Zr_{15}$	24	800	21	69
	$Al_{20}Cr_{25}Nb_{19}Ti_{20}Zr_{15}Y_1$	24	800	9	
	$Al_{10}CrNbTiZr_{10}$	50	1000	24	46
Ta-Alloy	TaMoCrTi	5	1000	0.9	70
	TaMoTiAl	5	1000	2.5	
	TaMoTi	5	1000	22	
	TaMoCrTiAll Si	48	1100	3.7	71
	TaMoCrTiAl	12	1100	10	72
Fe-alloys	HR120	1800	725	0.25	59
	310TaN	1800	725	0.35	
	HCM12A	1800	725	0.5	
	NF709	1800	725	0.8	
	HR3C	1800	725	0.15	
	347HFG	1800	725	0.9	
	Modified 800	1800	725	0.95	
	SAVE25	1800	725	1.15	
Other alloys	WMoCrTiAl	40	1000	8	73
	$13.4Ta_{20.3}Mo_{15.2}Nb_{25.2}Cr_{5.4}\ T_{117.6}Al_{2.9}Si$	100	1400	18	71
	CrMoNbTaV	25	1100	10	74

protection reduces the component weight and material consumption without sacrificing functionality.[78,79] There are some common coating techniques, such as laser cladding, magnetron sputtering, and high-velocity oxy-fuel, that have been widely used in various industries for anti-corrosion coating of HEAs. Table III shows some of the major high-entropy alloy coating techniques that are used in the steam corrosion environment. HEA has fair wettability on metallic substrates, and this enhances better adhesion and uniform coating coverage, leading to the formation of consistent and protective passive films on the substrate surface. Moreover, the refinement of the microstructure with minimized defects in the coatings enhances corrosion resistance. These synergistic effects can lead to better performance and extended service life of parts of biomedical implants and in components used in nuclear reactor and fuel cells.[80]

Various steels (304, AISI 1045, 316 l, etc.) are coated with HEAs such as FeCoCrNiTi, $AlCoCrFeNiMn_x$, $CoCrCu_{0.5}FeNiSi_x$, $Al_{0.3}CrFeCoNi$, CuCrFeMnNi, and (TiHfZrVNb)N (high-entropy alloy nitride) with a micrometer scale of thickness for improvement in high-temperature steam corrosion.[81–84] FeCoCrNiTi coatings were deposited on 304 stainless steel (304SS) substrates with a thickness ranging from 1.15 to 1.45 mm, enhancing its anti-tribocorrosion behavior. These coatings have an average grain size of 27.23 μm, which increases grain boundary density. This promotes the formation and repair of passive films and thereby enhances the corrosion resistance of the coatings.[3] AlCoCrFeNi coated on a 304 SS substrate with a thickness of 190–210 μm acts as an effective physical barrier with <1% porosity, against Cl^- ion attack on the substrate.[85] AISI 1045 steel was coated (1.2–1.5 mm) with $CoCrCu_{0.5}FeNiSi_x$, where increasing silicon (Si) content promoted the formation of silicide, aiding in refinement of the grains, thus enhancing corrosion resistance. HEA nitride coatings specifically (TiHfZrVNb)N with a thickness of 4.78 μm also showed significant improvement in the material's corrosion resistance.[86] The optimum interplay of parameters like coating thickness, microstructure control, and electrochemical properties ensures superior corrosion resistance.[87]

F. Elemental profile of HEAs during steam corrosion

HEAs before and after steam corrosion testing reveal critical insights into oxide layer formation, elemental segregation, and chemical bond transformations, with depth profiling. In Cr-containing HEAs, the formation of dense and adherent oxides (Cr_2O_3) occurs post high-temperature steam exposure at 300 °C. The formation of protective oxide barriers like CrO_3 or Al_2O_3 is linked to their elemental segregation in the oxide layer. The surface morphologies of the oxides formed on as-cast FeNiCrCuAl after exposure to supercritical water (SCW) at different temperatures and holding times are shown in Fig. 6. The oxide film grew along

TABLE III. Common HEA coating techniques.

Method	Coating type	Properties of coating/film	Advantages	Disadvantages
1. Thermal spraying	Thick coatings (100–300 μm)	- Dense (especially with HVOF) - Good adhesion - Can have oxides depending on environment - Low porosity - Mechanical bonding type	- Cost-effective - Suitable for large surfaces - Adjustable thickness - High scalability	- May have porosity - Oxidation during spraying - Rough surface
HVOF (high-velocity oxy-fuel)		- Dense, smooth coatings - Low porosity - Mechanical bonding type	- Lower oxidation - Strong mechanical bonding - High scalability	- Equipment cost - Requires careful parameter control
Plasma spraying		- Less dense than HVOF - Higher porosity - Metallurgical bonding type	- Suitable for high-temp HEAs - High deposition rates - High scalability	- Oxidation risk - Surface prep needed
2. Laser cladding	Thick coatings (200–500 μm)	- Dense, crack-free - Strong metallurgical bond - Good microstructure retention - Very low porosity	- Excellent bonding - Minimal dilution - Good corrosion resistance - Medium scalability	- High initial cost - Requires precise control - Slower process
3. Magnetron sputtering (PVD)	Thin films (1–10 μm)	- Nanocrystalline or amorphous structure - High purity - Very smooth and uniform - Very low porosity - Physical/atomic layering bonding type	- Precise composition control - Ideal for microelectronic/sensor applications - Low-medium scalability	- Expensive - Slow - Not suitable for thick coatings
4. Arc or RF Sputtering (PVD)		- High purity - Dense and uniform - Smooth surface - Very low porosity	- Good adhesion - Suitable for complex shapes - High scalability	- Low deposition rates - High vacuum requirements
5. Electrospark deposition (ESD)	Thin coatings (up to ~10 μm)	- Strong metallurgical bond - Rough surface - Microcracks possible - Low porosity	- Minimal heat input - Strong wear and corrosion resistance - Low scalability	- Limited thickness - Rough finish - Not suitable for large areas
6. Cold spraying	Thick coatings (~100 μm)	- Ductile coating - Low oxidation - Very low porosity - Nanostructure retained - Mechanical bonding type	- High deposition rate - No thermal degradation - Dense coatings - Medium-high scalability	- Limited to ductile powders - Requires high-pressure gas systems

the Cu-rich phase toward the interior of the substrate, and the embedding depth increased with temperature for a holding time of 100, 300, and 500 h, i.e., 2.84 ± 0.96 μm at 380 °C, 4.15 ± 0.56 μm at 500 °C, and 6.96 ± 0.94 μm at 650 °C, respectively.[48]

The elemental profiles and depth analysis of the FeNiCrCuAl were studied using TEM with energy dispersive x-ray spectroscopy (EDS) line scans (Fig. 8). Cross-sectional view of the oxide layer formed on the pristine HEA after 300 hours of exposure to supercritical water (SCW). First, in the FeCr-rich BCC regions, after 100 h at 550 °C and 25 MPa in SCW, a duplex oxide structure formed, featuring an outer $FeAl_2O_4$ spinel layer (~1 μm) and an inner $FeCr_2O_4$ spinel layer (~200 nm), with Cu_2O particles embedded. Second, post-1000 h, the oxide evolved into an outer γ-Al_2O_3 layer and an inner $CrAl_2O_4$ spinel layer, with Cr_2O_3 particles appearing beneath. In the NiAl-rich BCC regions, a stable duplex oxide structure was observed at both 100 and 1000 h, comprising an outer γ-Al_2O_3 layer (0.32–1.1 μm) and an inner $NiAl_2O_4$ layer, developed on the NiAl-rich regions regardless of the exposure period. In the Cu-rich FCC regions, localized corrosion caused redeposition of Cu_2O particles on the surface.[42] In FeNiCrCuAl exposure to 380 °C SCW, oxide particles such as irregular Cu_2O, Al_2O_3 stripes, and $FeCr_2O_4$/$(Al,Fe)_3O_4$ polyhedra formed on NiAl-rich and FeCr-rich regions, with Cu_2O and $FeCr_2O_4$ particle sizes increasing over time (100–500 h). Duplex and triplex oxide

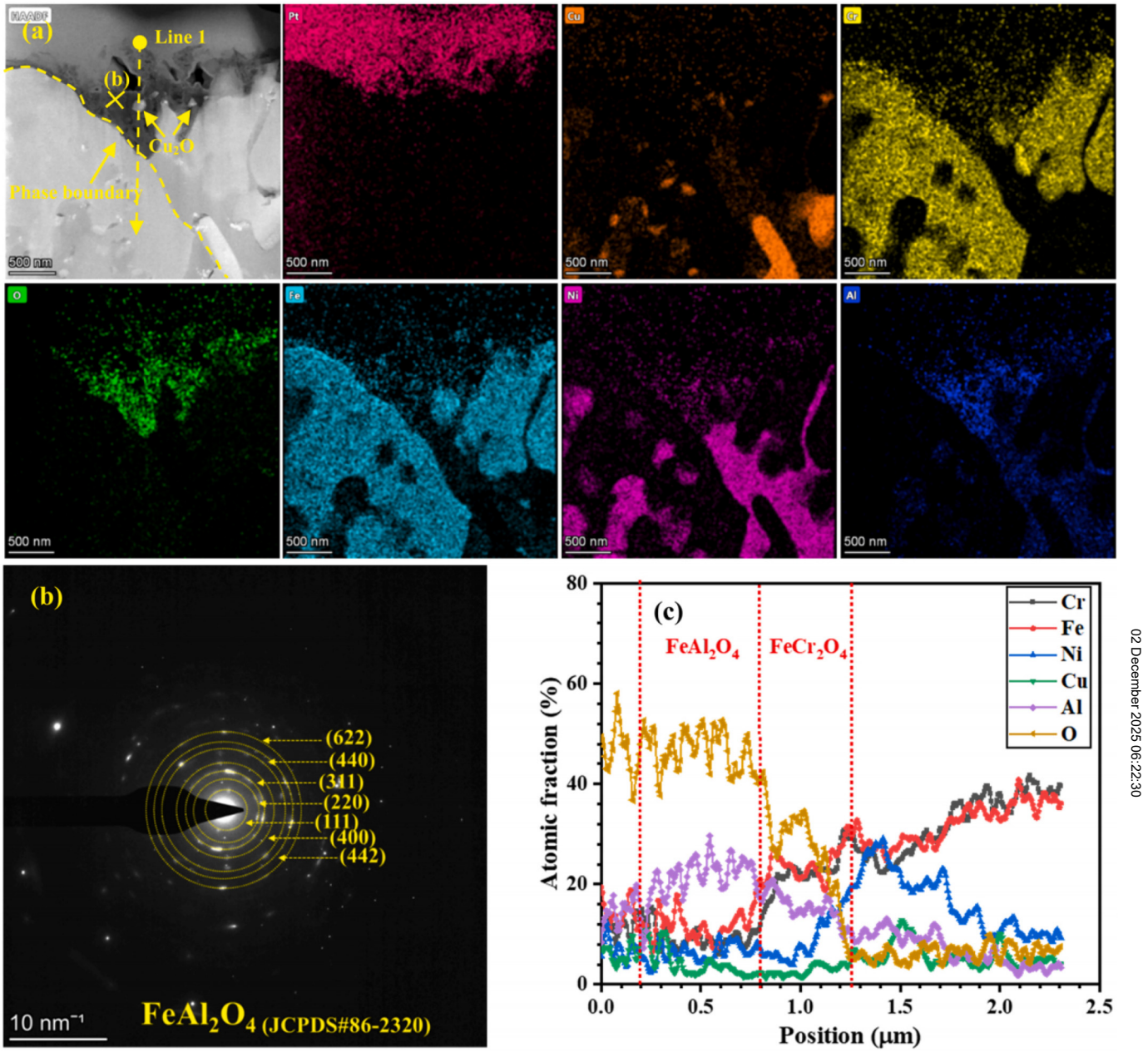

FIG. 8. Cross section of the oxide layer of pristine HEA after 300 h exposure to SCW: (a) TEM image and corresponding EDS elemental maps; (b) the selected area electron diffraction (SAED) pattern of the Cr-rich oxide film; and (c) the EDS compositional profile of O, Cr, Fe, Co, and Ni.[42] Reproduced with permission from Huang *et al.*, Corros. Sci. **208**, 1–14 (2022). Copyright 2022 Elsevier.

films were developed with varying layer compositions and thicknesses (~2.60 and ~0.97 μm). At 500 °C, similar morphologies were observed, though oxide particle sizes and film thicknesses slightly increased. At 650 °C, Al_2O_3 oxides became significantly larger and denser, while Cu_2O particles decreased in size. Distinct multi-layered oxide structures formed on NiAl- and FeCr-rich regions, with oxide film thicknesses of ~2.90 and ~0.90 μm, respectively.[45]

The graphene-reinforced laminated CoCrFeNiMn showed a uniform distribution of Co, Cr, Fe, Ni, and Mn within the FCC matrix, along with localized Cr- and Mn-rich oxides mainly in the slurry regions due to pre-oxidation during processing. After 100 h

of steam oxidation at 1000 °C, a multi-layered oxide scale formed, featuring an inner Cr-rich Cr_2O_3 layer and an outer Mn-rich $(Mn,Cr)_3O_4/Mn_3O_4$ layer. Cross-sectional EDS revealed that the Mn and Cr get depleted near the oxide/matrix interface from outward diffusion, while oxygen penetration caused internal oxidation within the matrix. Elemental depth profiling confirmed Cr enrichment in the inner oxide layer and Mn depletion in the substrate, with GNPs largely intact due to their parallel alignment, which contributed to the composite's enhanced oxidation resistance.[88]

IV. FACTORS INFLUENCING CORROSION RESISTANCE

The steam corrosion resistance of (HEAs) is intricately influenced by multiple factors. Figure 9 shows the factors affecting corrosion properties. First and foremost, the alloy composition plays a pivotal role in shaping their resistance to steam-induced corrosion. Furthermore, the sluggish diffusion effect of HEAs and the complex atomic arrangement impede the movement of corrosive species, reducing their ability to penetrate the material and form a stable and protective oxide layer on the surface are paramount, acting as a barrier against further degradation in the presence of steam. Sensitivity to temperature and pressure conditions is another critical aspect, with the alloy's performance varying under diverse steam environments, necessitating optimization for specific temperature and pressure ranges. Microstructure stability, including the presence of multiple phases and grain boundaries, also contributes to the alloy's resilience against steam-induced degradation. Some HEAs exhibit passivation, forming a protective layer that inhibits corrosion, adding to their overall resistance. The distribution of alloying elements within the microstructure and the surface

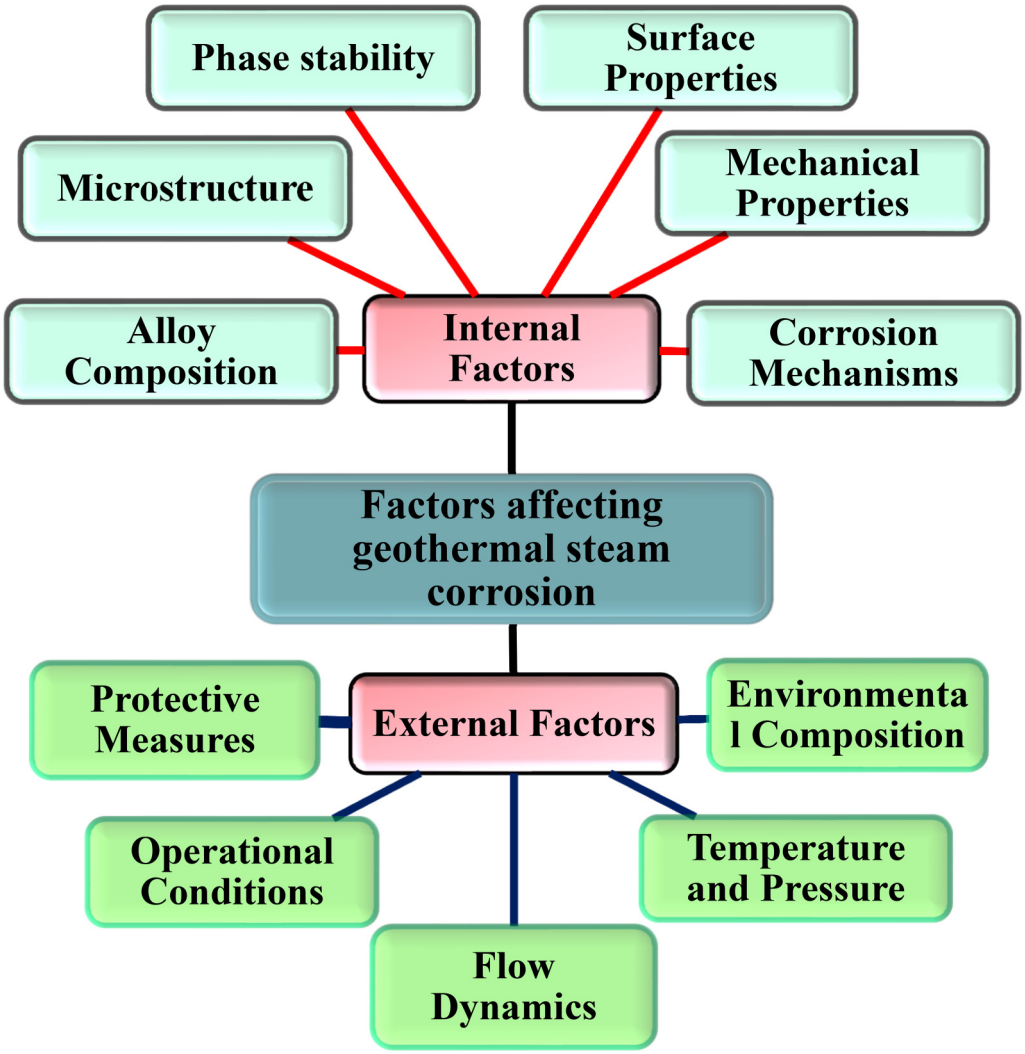

FIG. 9. Factors affecting corrosion properties.

finish and condition are crucial, impacting susceptibility to steam corrosion. Exposure time is a critical factor, as some HEAs may show excellent short-term resistance but could experience degradation over extended periods. Finally, the presence of impurities in steam, such as contaminants or aggressive species, can affect corrosion resistance, necessitating HEAs designed for specific impurity-laden steam environments. The optimization of these factors through meticulous alloy design, processing, and testing is essential for developing high-entropy alloys with superior steam corrosion resistance, rendering them suitable for applications in steam-rich environments, including power generation systems. In addition to this, factors influencing corrosion resistance are categorized into two based on their origin.

The transition from laboratory research to industrial deployment of corrosion-resistant HEAs for geothermal systems faces several critical challenges. Lab-produced HEAs can be disks, rods, pellets, thin films, or small blocks, and their typical weight ranges from a few grams to several hundred grams. While thin films range in thickness from 10 nm to a few micrometers, lab-scale ingots or buttons typically measure between 10 and 50 mm in diameter and 5–20 mm in thickness. Bulk samples made by casting or sintering can have lengths or diameters ranging from 10 to 100 mm, while powders at this scale are typically in the micrometer to sub-micrometer range. Industrial-scale HEAs, on the other hand, are made in far greater quantities, from a few kilograms to tons, and come in a variety of forms, including powders, rolled sheets, forged parts, cast components, rods, and wires. Industrial ingots are 100–500 mm in diameter and up to 1 m long; rods and bars are usually 10–100 mm in diameter and several meters long, and sheets or plates can be 1–20 mm thick, up to 1 m wide, and several meters long. Additionally, powders are made in large quantities for uses such as coatings and additive manufacturing.[89,90]

A primary obstacle is the difficulty in scaling lab results to actual geothermal environments. HEAs must withstand complex, multi-factor degradation mechanisms, including high-temperature corrosion, stress corrosion cracking, and erosion–corrosion under dynamic flow conditions.[91–93] The lack of long-term field-testing data is another significant limitation since most studies rely on short-term laboratory tests that are unable to predict material behavior. Faster cooling rates during lab-scale production encourage finer microstructures, which improve corrosion resistance through efficient mixing. On the other hand, slower cooling in large-scale production, combined with less efficient mixing, can lead to composition gradients, segregation, and the formation of coarse grains.[17,18] Additively manufactured HEAs frequently have significantly higher corrosion resistance than their arc-melted counterparts due to variations in microstructural features such as porosity, elemental segregation, and residual stresses. For instance, laser powder bed fusion of AlCoCrFeNi alloys has been shown to produce finer microstructures than conventionally cast versions of the same alloy.[94–96]

V. FUTURE DIRECTIONS

Several future directions have been identified to enhance performance in steam-rich environments. These include a dedicated focus on refining and optimizing HEA compositions for superior steam corrosion resistance, emphasizing the selection of alloying elements that form protective oxide layers. Advanced microstructure engineering techniques are under exploration to tailor the internal structure of HEAs, ensuring improved resistance to steam-induced corrosion by optimizing grain boundaries and phase distributions. The diffusion pathway and diffusion barrier created by a multi-grain structure, variation in grain sizes (micro- and nano-grains), or a dual-phase structure in high-entropy alloys can effectively hinder or block the diffusion pathway. This can slow down diffusion reactions by increasing the complexity of the diffusion process.

The presence of diverse grain sizes and dual-phase structures introduces a unique variation in interfaces and boundaries, which act as obstacles to atomic movement. These features reduce the diffusivity of atoms, making the material more resistant to diffusion-driven phenomena such as corrosion, oxidation, and phase transformations. Figure 10 illustrates the morphology and structure of the microstructure, collectively providing insights into the crystallographic features of the high-entropy alloy. These features are directly related to how multi-grain structures, varied grain sizes, and dual-phase distributions create diffusion barriers and slow down diffusion reactions. Additionally, innovative surface modification methods like coatings or treatments are being investigated to create protective layers on HEA surfaces, mitigating the impact of steam exposure.

The development of *in situ* corrosion monitoring techniques during HEA synthesis and service aims to enable real-time assessment of corrosion behavior, providing a comprehensive understanding of how HEAs respond to steam exposure over time. Establishing standardized and rigorous testing protocols for evaluating HEAs under high-temperature steam conditions is critical, offering a consistent benchmark for assessing the steam corrosion resistance of different alloy formulations.

Multi-scale modeling approaches are being employed to simulate the behavior of HEAs under steam corrosion conditions, aiding in predicting performance, optimizing compositions, and understanding complex interactions at different scales. Targeted research for specific applications, such as power generation systems or steam turbines, involves tailoring HEA properties based on unique challenges posed by these environments.

Machine learning (ML) in HEA anti-corrosion design focuses on developing hybrid physics-informed models that combine the density functional theory (DFT) simulations and neural networks to predict phase stability, while active learning systems enable autonomous alloy development through closed-loop synthesis and testing.[98–100] ML, thermodynamic modeling, and high-throughput computational tools are exploited to discover high-temperature oxidation-resistant HEAs for advanced turbine systems. Dataset of K_p values (oxidation parabolic rate constants) was compiled from over 106 papers, covering 340 alloy compositions. 44 features were used, including elemental compositions, phase stability parameters (Ω, δ, ΔH_{mix}), and Cr/Al ratios to predict high-temperature oxidation-resistant HEAs.[101] By integrating several ML techniques such as Logistic Regression (LR), Decision Tree (DT), Random Forest (RF), K-Nearest Neighbor (KNN), Artificial Neural Network (ANN), and Synthetic Minority Over-sampling Technique (SMOTE), prediction of the cracks of oxide scales during high-

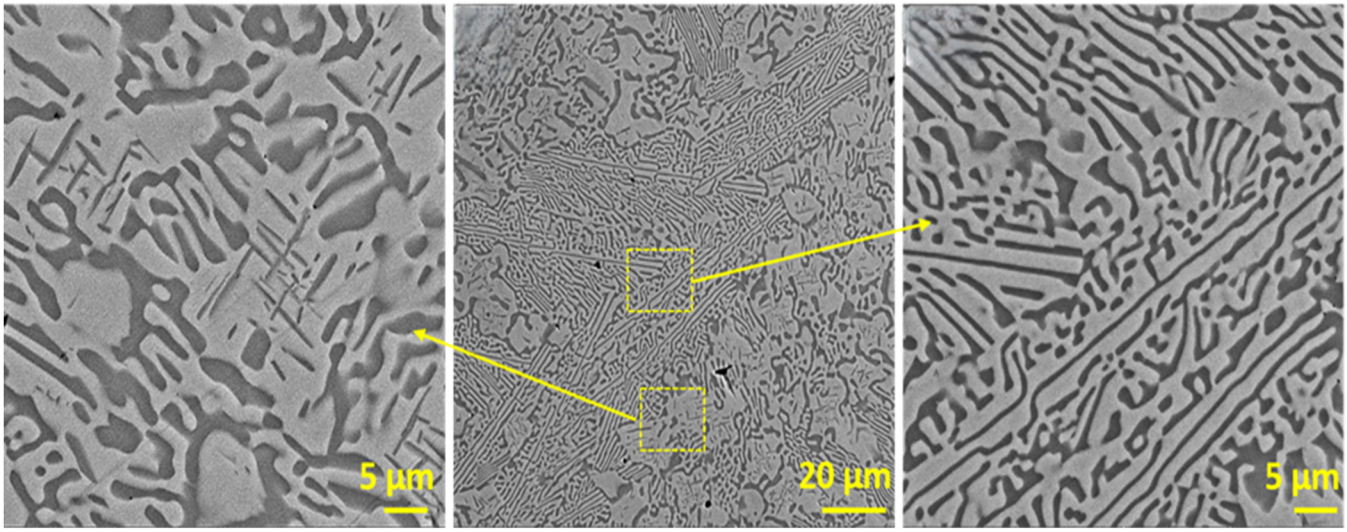

FIG. 10. Multi-scale hierarchical microstructure of $(NiCo)_{1.7}AlCrFe$ HEA.[97] Reproduced with permission from Vikram *et al.*, Philos. Mag. **103**(16), 1592–1602 (2023). Copyright 2023 Taylor and Francis.

temperature oxidation of metals and alloys can be done.[102] To discover Cr- and Al-containing HEAs with high oxidation resistance at 1100 °C in air, ML was applied to 482 datasets from the literature containing chemical compositions, oxidation temperature/time, and weight gain after exposure. Nine algorithms were tested, identifying AlCrCuFeNi as a top-performing HEA.[103] ML was used to predict the corrosion behavior of the HfNbTaTiZr system in simulated body fluid (SBF) at 37 ± 1 °C, based on data from 46 HEAs reported in the literature, all vacuum arc-melted and tested in the as-cast form. The target variable was corrosion potential (E_{corr}), chosen over corrosion current due to reproducibility issues. The dataset included 12 elemental/experimental features and 22 calculated features (e.g., VEC, δr, Δχ, ΔH, ΔS, etc.).[104]

Several research groups have standardized microstructural, electrochemical, and operando datasets, which aid artificial intelligence (AI) tools such as Shapley Additive Models (SHAPs) to analyze corrosion mechanisms and establish design rules while addressing challenges in multi-scale data integration. Optimizing resource efficiency through element substitution strategies and using Generative Adversarial Network (GAN)-generated synthetic data to simulate extreme environments is practiced in the ML study domain. AI approaches will turn ML from a predictive tool into a self-driving platform for next-generation corrosion-resistant HEAs that can withstand the most aggressive operating conditions.[105]

VI. CONCLUSION

The review highlights the potential of high-entropy alloys as novel materials for components in harsh steam environments encountered in power generation systems, nuclear facilities, and geothermal applications. HEAs demonstrate superior steam corrosion resistance compared to traditional alloys due to their unique composition, complex atomic arrangements, and passivation behavior.

- Adjusting the proportions of specific elements within HEAs can trigger phase changes, forming novel alloy systems. For example, increasing the concentration of elements like chromium (Cr) and aluminum (Al) can lead to the emergence of Lave phases, enhancing properties such as corrosion resistance.
- The distribution of phase structures in steam corrosion-resistant alloys varies, with 45.2% of HEAs exhibiting FCC structures, 35.5% displaying BCC structures, and 19.4% comprising a combination of these phases. Notably, alloys with FCC and combined FCC + BCC structures demonstrate superior resistance to high-temperature steam corrosion compared to those with BCC structures.
- $Al_{25}Co_{25}Cr_{25}Ni_{25}$ HEA exhibits remarkable oxidation resistance at 1000 °C in steam vapor environments, making it suitable for dynamic thermal environments.

AUTHOR DECLARATIONS

Conflict of Interest

The authors have no conflicts to disclose.

Author Contributions

Amal Sasi: Data curation (equal); Investigation (equal); Software (equal); Writing – original draft (equal); Writing – review & editing (equal). **R. J. Vikram:** Supervision (equal); Writing – review & editing (supporting). **K. Dash:** Conceptualization (equal); Data curation (equal); Software (equal); Supervision (equal);

Validation (equal); Writing – original draft (equal); Writing – review & editing (equal).

DATA AVAILABILITY

The data that support the findings of this study are available from the corresponding author upon reasonable request.

REFERENCES

[1]G. R. Holcomb, B. S. Covino, Jr., S. J. Bullard, S. D. Cramer, and M. Z. Moroz, "Ultra supercritical steamside oxidation," in *Corrosion 2005, Houston, Texas, 3-7 April 2005,* Paper No. NACE-05398 (2005); available at https://onepetro.org/NACECORR/proceedings-abstract/CORR05/All-CORR05/NACE-05398/115346

[2]T. Dudziak, K. Jura, A. Polkowska, V. Deodeshmukh, M. Warmuzek, M. Witkowska, W. Ratuszek, and K. Chruściel, "Steam oxidation resistance of advanced steels and Ni-based alloys at 700 °C for 1000 h," Oxid. Met. **89**(5–6), 755–779 (2018).

[3]A. Fry, S. Osgerby, and M. Wright, "Oxidation of alloys in steam environments—A review," NPL Report No. MATC(A)90 (National Physics Laboratory, 2002).

[4]K. Nakamura, Y. Shimada, T. Miyashita, A. Serizawa, and T. Ishizaki, "Effect of vapor pressure during the steam coating treatment on structure and corrosion resistance of the $Mg(OH)_2$/Mg-Al LDH composite film formed on Mg alloy AZ61," Materials **11**(9), 1659 (2018).

[5]T. Li, D. Wang, S. Zhang, and J. Wang, "Corrosion behavior of high entropy alloys and their application in the nuclear industry—An overview," Metals **13**(2), 1–10 (2023).

[6]G. R. Holcomb, D. E. Alman, Ő. N. Doğan, J. C. Rawers, K. K. Schrems, and M. Ziomek-Moroz, "Steam turbine materials and corrosion," in *Conference: 22nd Annual Conference on Fossil Energy Materials, Pittsburgh, PA, 8–10 July 2008* (National Energy Technology Laboratory, 2008).

[7]X. Yongli *et al.*, "The material corrosion under supercritical and high temperature steam conditions (short literature survey)" (1994).

[8]A. Nurrochman, E. Junianto, A. A. Korda, B. Prawara, and E. A. Basuki, "Research hotspots and future trends of hot corrosion research: A bibliometric analysis," RSC Adv. **13**(43), 29904–29922 (2023).

[9]R. Bertani, "Geothermal power generation in the world 2005–2010 update report," Geothermics **41**, 1–29 (2012).

[10]R. Bertani, "Geothermal power generation in the world 2010–2014 update report," Geothermics **60**, 31–43 (2016).

[11]G. W. Huttrer, "The status of world geothermal power generation 1995 ± 2000," Geothermics **30**, 1–27 (2001).

[12]W. F. Giggenbach *et al.*, "Geothermal gas equilibria," Geochim. Cosmochim. Acta **44**(12), 2021–2032 (1980).

[13]G. He *et al.*, "Corrosion mechanism of high temperature and O_2 content in steamed CO_2," Process Saf. Environ. Prot. **163**, 7 (2022).

[14]J. Nogara and S. J. Zarrouk, "Corrosion in geothermal environment: Part 1: Fluids and their impact," Renew. Sustain. Energy Rev. **82**, 1333–1346 (2018).

[15]T. Kaya, P. Hoşhan, O. Jeotermal Mühendislik, S. ve Ticaret AŞAnkara, and T. Araştırma Merkezi, "Corrosion and material selection for geothermal systems," in *Proceedings World Geothermal Congress, Antalya, Turkey, 24–29 April 2005* (Geothermal Rising, 2005).

[16]G. A. El-Awadi, S. Abdel-Samad, and E. S. Elshazly, "Hot corrosion behavior of Ni based Inconel 617 and Inconel 738 superalloys," Appl. Surf. Sci. **378**, 224–230 (2016).

[17]B. Ganesh Reddy Majji, H. Vasudev, and A. Bansal, "A review on the oxidation and wear behavior of the thermally sprayed high-entropy alloys," Mater. Today Proc. **50**, 1447–1451 (2021).

[18]Y. Zhang, T. T. Zuo, Z. Tang, M. C. Gao, K. A. Dahmen, P. K. Liaw, and Z. P. Lu, "Microstructures and properties of high-entropy alloys," Prog. Mater. Sci. **61**, 1–93 (2014).

[19]X. Zhou *et al.*, "A review on fundamental of high entropy alloys with promising," J. Alloys Compd. **760**, 9 (2018).

[20]E. P. George *et al.*, "High entropy alloys: A focused review of mechanical properties and deformation mechanisms," Acta Mater. **188**, 435–474 (2020).

[21]Y. Shi, B. Yang, and P. K. Liaw, "Corrosion-resistant high-entropy alloys: A review," Metals **7**(2), 1–29 (2017).

[22]S. Rajendrachari, "An overview of high-entropy alloys prepared by mechanical alloying followed by the characterization of their microstructure and various properties," Alloys **1**(2), 116–132 (2022).

[23]R. Sabban, K. Dash, S. Suwas, and B. S. Murty, "Strength–ductility synergy in high entropy alloys by tuning the thermo-mechanical process parameters: A comprehensive review," J. Indian Inst. Sci. **102**(1), 91–116 (2022).

[24]M. A. Jafar Mazumder, "Global impact of corrosion: Occurrence, cost and mitigation," Glob. J. Eng. Sci. **5**(4), 344–352 (2020).

[25]M. V. Biezma and J. R. San Cristóbal, "Methodology to study cost of corrosion," Corros. Eng. Sci. Technol. **40**(4), 344–352 (2005).

[26]See http://impact.nace.org/economic-impact.aspx for "The Effects and Economic Impact of Corrosion."

[27]P. V. Ananthapadmanabhan, K. P. Sreekumar, K. V. Muraleedharan, and N. Venkatramani, "Plasma-sprayed composite coatings for high temperature applications," Surf. Coat. Technol. **49**, 62–66 (1991).

[28]V. Chawla, A. Chawla, D. Puri, S. Prakash, P. G. Gurbuxani, and B. Singh Sidhu, "Hot corrosion & erosion problems in coal based power plants in India and possible solutions—A review," J. Miner. Mater. Character. Eng. **10**(04), 367–386 (2011).

[29]S. Harsimran, K. Santosh, and K. Rakesh, "Overview of corrosion and its control: A critical review," Proc. Eng. Sci. **3**(1), 13–24 (2021).

[30]B. Raj and U. K. Mudali, "Materials science and technology: Research and challenges in nuclear fission power," Proc. Ind. Natl. Sci. Acad. **81**(4), 801–826 (2015).

[31]R. S. Dutta, "Corrosion aspects of Ni–Cr–Fe based and Ni–Cu based steam generator tube materials," J. Nucl. Mater. **393**(2), 343–349 (2009).

[32]X. Guo, P. Lai, L. Li, L. Tang, and L. Zhang, "Progress in studying the fretting wear/corrosion of nuclear steam generator tubes," Ann. Nucl. Energy **144**, 0306–4549 (2020).

[33]Q. Shen, J. Xue, X. Yu, Z. Zheng, and N. Ou, "Triple-wire plasma arc cladding of Cr–Fe–Ni–Ti_x high-entropy alloy coatings," Surf. Coat. Technol. **443**, 128638 (2022).

[34]P. Bi, N. Hashimoto, S. Hayashi, H. Oka, and S. Isobe, "Effect of Al on oxidation behavior of $Al_xCrCuFeNi_2$ (x = 0.2, 0.4, 0.6) high entropy alloys," Corros. Sci. **208**, 060–8628 (2022).

[35]C. Xiang, H. M. Fu, Z. M. Zhang, E. H. Han, H. F. Zhang, J. Q. Wang, and G. D. Hu, "Effect of Cr content on microstructure and properties of $Mo_{0.5}VNbTiCr_x$ high-entropy alloys," J. Alloys Compd. **818**, 153352 (2020).

[36]F. Liu, P. K. Liaw, and Y. Zhang, "Recent progress with BCC-structured high-entropy alloys," Metals **12**(3), 1–23 (2022).

[37]Z. Cai, F. Jiang, N. Wei, L. Mi, C. Zhang, X. Liu, F. Si, and T. Wu, "Effect of annealing temperatures on phase stability, mechanical properties, and high-temperature steam corrosion resistance of $(FeNi)_{67}Cr_{15}Mn_{10}Al_5Ti_3$ alloy," Metals **12**(9), 1–14 (2022).

[38]Z. Tang, S. Zhang, R. Cai, Q. Zhou, and H. Wang, "Designing high entropy alloys with dual fcc and bcc solid-solution phases: Structures and mechanical properties," Metall. Mater. Trans. A Phys. Metall. Mater. Sci. **50**(4), 1888–1901 (2019).

[39]U. Hecht, S. Gein, O. Stryzhyboroda, E. Eshed, and S. Osovski, "The BCC-FCC phase transformation pathways and crystal orientation relationships in dual phase materials from Al–(Co)–Cr–Fe–Ni alloys," Front. Mater. **7**, 7 (2020).

[40]X. L. Shang, Z. J. Wang, F. He, J. C. Wang, J. J. Li, and J. K. Yu, "The intrinsic mechanism of corrosion resistance for FCC high entropy alloys," Sci. China Technol. Sci. **61**(2), 189–196 (2018).

[41]C. Tang, H. Shi, A. Jianu, A. Weisenburger, G. Victor, M. Grosse, G. Müller, H. J. Seifert, and M. Steinbrück, "High-temperature oxidation of AlCrFeNi-(Mn or Co) high-entropy alloys: Effect of atmosphere and reactive element addition," Corros. Sci. **192**, 109809 (2021).

[42]A. I. Thorhallsson, I. Csáki, L. E. Geambazu, F. Magnus, and S. N. Karlsdottir, "Effect of alloying ratios and Cu-addition on corrosion behaviour of

CoCrFeNiMo high-entropy alloys in superheated steam containing CO_2, H_2S and HCl," Corros. Sci. **178**, 109083 (2021).
[43]X. Huang, Z. Zhan, Q. Zhao, J. Liu, L. Wei, and X. Li, "Corrosion behavior of a dual-phase FeNiCrCuAl high entropy alloy in supercritical water," Corros. Sci. **208**, 110617 (2022).
[44]S. N. Karlsdottir, I. Csaki, I. V. Antoniac, C. A. Manea, R. Stefanoiu, F. Magnus, and F. Miculescu, "Corrosion behavior of AlCrFeNiMn high entropy alloy in a geothermal environment," Geothermics **81**, 32–38 (2019).
[45]Q. Zhao, X. Huang, Z. Zhan, S. Zhou, X. He, H. Huang, P. Zhu, L. Wei, X. Li, and Y. Xie, "Effect of exposure temperature on the corrosion behavior of a FeNiCrCuAl high entropy alloy in supercritical water," Corros. Sci. **227**, 1–15 (2024).
[46]H. Shi, C. Tang, A. Jianu, R. Fetzer, A. Weisenburger, M. Steinbrueck, M. Grosse, R. Stieglitz, and G. Müller, "Oxidation behavior and microstructure evolution of alumina-forming austenitic & high entropy alloys in steam environment at 1200 °C," Corros. Sci. **170**, 1–13 (2020).
[47]H. He, M. Lai, C. Liu, G. Zeng, L. He, W. Zhang, J. Yi, S. Liu, and J. Long, "Effects of deposition temperature on the microstructure, mechanical properties, high temperature corrosion and oxidation properties of AlCrNbTiZr high entropy alloy coatings," Int. J. Refract. Met. Hard Mater .**112**, 0263-4368 (2023).
[48]Z. Cai, N. Wei, Y. Han, F. Si, L. Mi, C. Zhang, X. Liu, F. Jiang, and T. Wu, "Effect of heat treatment on microstructure, tensile properties and high-temperature corrosion resistance of the FeCrMnNi high entropy alloy," Metals **12**(9), 1–16 (2022).
[49]Q. Zhao, X. Huang, Z. Zhan, S. Zhou, X. He, H. Huang, P. Zhu, L. Wei, X. Li, and Y. Xie, "Effect of exposure temperature on the corrosion behavior of a FeNiCrCuAl high entropy alloy in supercritical water," Corros. Sci. **227**, 1–15 (2024).
[50]X. Wang, Z. Zeng, H. Wang, H. Bai, W. Li, Y. Li, Z. Wang, Y. Chen, and B. Yang, "Effect of bias voltage on structure, mechanical properties, and high-temperature water vapor corrosion of AlCrNbSiTi high entropy alloy coatings," Coatings **13**(11), 1–14 (2023).
[51]Q. Zhao, X. Huang, Z. Zhan, S. Zhou, J. Liu, P. Zhu, L. Wei, X. Li, C. Li, and Y. Xie, "Effect of alloying elements (Mn, Ti, and Mo) on the corrosion behavior of FeCoNiCr-based high entropy alloy in supercritical water," Corros. Sci. **220**, 111291 (2023).
[52]C. Liu, X. Jiang, H. Sun, T. Liu, Z. Wu, and L. Yang, "Steam oxidation properties of graphene reinforced bioinspired laminated CoCrFeNiMn high-entropy alloy matrix composites at 1000 °C," Mater. Today Commun. **38**, 107962 (2024).
[53]R. Gawel, Ł. Rogal, G. Smoła, C. Zhou, and Z. Grzesik, "The influence of water vapour on high-temperature oxidation of Al, Co, Cr, Ni-containing high entropy alloys under thermal shock conditions," J. Alloys Compd. **952**, 170054 (2023).
[54]S. Abbaszadeh, A. Pakseresht, H. Omidvar, and A. Shafiei, "Investigation of the high-temperature oxidation behavior of the $Al_{0.5}$CoCrFeNi high entropy alloy," Surf. Interfaces **21**, 100724 (2020).
[55]G. R. Holcomb, J. Tylczak, and C. Carney, "Oxidation of CoCrFeMnNi high entropy alloys," J. Mater. **67**(10), 2326–2339 (2015).
[56]X. X. Yu, M. A. Taylor, J. H. Perepezko, and L. D. Marks, "Competition between thermodynamics, kinetics and growth mode in the early-stage oxidation of an equimolar CoCrFeNi alloy," Acta Mater. **196**, 651–659 (2020).
[57]R. Gawel, Ł Rogal, and Z. Grzesik, "Behaviour of Al, Co, Cr, Ni-based high entropy alloys under high-temperature thermal shock oxidising conditions," Corros. Sci. **198**, 110116 (2022).
[58]L. E. Geambazu, C. A. Manea, I. Csaki, and F. Miculescu, "$Al_{0.5}$CrCoFeNi high entropy alloy for geothermal environment," in *IOP Conference Series: Materials Science Engineering* (Institute of Physics Publishing, 2019).
[59]K. Natesan *et al.*, see https://www.osti.gov/biblio/835676 for "Coal-ash Corrosion of Alloys for Combustion Power Plants *."
[60]P. Wales and M. Pourbaix, "Atlas D'Equilibres Electro-chemiques," J. Electrochem. Soc. **111**(1), 1116–1121 (1956).
[61]O. N. Senkov, S. V. Senkova, D. M. Dimiduk, C. Woodward, and D. B. Miracle, "Oxidation behavior of a refractory $NbCrMo_{0.5}Ta_{0.5}TiZr$ alloy," J. Mater. Sci. **47**(18), 6522–6534 (2012).
[62]C. M. Liu, H. M. Wang, S. Q. Zhang, H. B. Tang, and A. L. Zhang, "Microstructure and oxidation behavior of new refractory high entropy alloys," J. Alloys Compd. **583**, 162–169 (2014).
[63]B. Gorr, F. Mueller, H. J. Christ, T. Mueller, H. Chen, A. Kauffmann, and M. Heilmaier, "High temperature oxidation behavior of an equimolar refractory metal-based alloy 20Nb—20Mo—20Cr—20Ti—20Al with and without Si addition," J. Alloys Compd. **688**, 468–477 (2016).
[64]F. Müller, B. Gorr, H. J. Christ, H. Chen, A. Kauffmann, and M. Heilmaier, "Effect of Y additions on the oxidation behaviour of novel refractory high-entropy alloy NbMoCrTiAl at 1000 °C in air," Oxid. Met. **94**(1–2), 147–163 (2020).
[65]M. Ghadyani, C. Utton, and P. Tsakiropoulos, "Microstructures and isothermal oxidation of the alumina scale forming $Nb_{1.45}Si_{2.7}Ti_{2.25}Al_{3.25}Hf_{0.35}$ and $Nb_{1.35}Si_{2.3}Ti_{2.3}Al_{3.7}Hf_{0.35}$ alloys," Materials **12**(5), 759 (2019).
[66]O. A. Waseem, U. Auyeskhan, H. M. Lee, and H. J. Ryu, "A combinatorial approach for the synthesis and analysis of $Al_xCr_yMo_zNbTiZr$ high-entropy alloys: Oxidation behavior," J. Mater. Res. **33**(19), 3226–3234 (2018).
[67]N. Yurchenko, E. Panina, S. Zherebtsov, G. Salishchev, and N. Stepanov, "Oxidation behavior of refractory $AlNbTiVZr_{0.25}$ high-entropy alloy," Materials **11**(12), 2526 (2018).
[68]Y. Du, D. Ding, L. Lai, S. Xiao, N. Guo, B. Song, and S. Guo, "Effect of Y on the high-temperature oxidation behavior of CrMoTaTi refractory high entropy alloy," Int. J. Refract. Met. Hard Mater. **103**, 0263–4368 (2022).
[69]L. Chen, X. Zhang, Y. Wang, X. Hao, and H. Liu, "Microstructure and elastic constants of AlTiVMoNb refractory high-entropy alloy coating on Ti6Al4V by laser cladding," Mater. Res. Express **6**(11), 1–11 (2019).
[70]L. C. Li, M. X. Li, M. Liu, B. Y. Sun, C. Wang, J. T. Huo, W. H. Wang, and Y. H. Liu, "Enhanced oxidation resistance of MoTaTiCrAl high entropy alloys by removal of Al," Sci. China Mater. **64**(1), 223–231 (2021).
[71]B. Gorr, S. Schellert, F. Müller, H. J. Christ, A. Kauffmann, and M. Heilmaier, "Current status of research on the oxidation behavior of refractory high entropy alloys," Adv. Eng. Mater. **23**(5), 1–14 (2021).
[72]F. Müller, B. Gorr, H. J. Christ, J. Müller, B. Butz, H. Chen, A. Kauffmann, and M. Heilmaier, "On the oxidation mechanism of refractory high entropy alloys," Corros. Sci. **159**, 108161 (2019).
[73]B. Gorr, F. Müller, M. Azim, H. J. Christ, T. Müller, H. Chen, A. Kauffmann, and M. Heilmaier, "High-temperature oxidation behavior of refractory high-entropy alloys: Effect of alloy composition," Oxid. Met. **88**(3–4), 339–349 (2017).
[74]Y. Xiao, W. Kuang, Y. Xu, L. Wu, W. Gong, J. Qian, Q. Zhang, and Y. He, "Microstructure and oxidation behavior of the CrMoNbTaV high-entropy alloy," J. Mater. Res. **34**(2), 301–308 (2019).
[75]S. Caramarin, I. C. Badea, L. F. Mosinoiu, D. Mitrica, B. A. Serban, N. Vitan, L. M. Cursaru, and A. Pogrebnjak, "Structural particularities, prediction, and synthesis methods in high-entropy alloys," Appl. Sci. **14**(17), 1–20 (2024).
[76]L. F. Mosinoiu, A. Sobetkii, B. A. Serban, L. M. Cursaru, A. C. Matei, M. Ghita, N. Vitan, S. Caramarin, D. Mitrica, A. Pogrebnjak, and B. Postolnyi, "Chemical and structural characteristics of copper added high entropy alloys for corrosive applications," J. Mater. Res. Technol. **35**, 6261–6268 (2025).
[77]X. Zhang, V. Pelenovich, X. Zeng, Q. Wan, J. Liu, A. Pogrebnjak, Y. Guo, Y. Liu, Y. Lei, and B. Yang, "Unravel hardening mechanism of AlCrNbSiTi high-entropy alloy coatings," J. Alloys Compd. **965**, 171222 (2023).
[78]A. D. Pogrebnjak, A. A. Bagdasaryan, I. V. Yakushchenko, and V. M. Beresnev, "The structure and properties of high-entropy alloys and nitride coatings based on them," Russ. Chem. Rev. **83**(11), 1027–1061 (2014).
[79]K. X. Zheng, D. T. Yu, J. L. Liu, C. L. Wu, S. Zhang, C. H. Zhang, Q. Wang, and D. Zhang, "Laser cladding of FeCoCrNiTi high-entropy alloy coatings to modulate the microstructure and enhance the tribo-corrosion behavior on 304 stainless steel," Surf. Coat. Technol. **505**, 132114 (2025).
[80]H. T. Hassan, "Antibody-drug conjugate [ADC] treatment of leukaemia," Leukemia Res. **131**, 107078 (2023).

[81]R. Tyagi, B. D. Y. Sunil, M. Kumar, H. Bishwakarma, K. K. Saxena, R. Chandrashekar, J. Ali, L. Sehgal, and A. A. Lakshmi, "Micro-electrical discharge coating of AlCoCrFeNi high entropy alloy on MgAz31B to enhance the corrosion and wear resistance," Res. Surf. Interfaces **19**, 100493 (2025).
[82]B. Dikici, T. Lindner, E. Şakar, L. Lampke, D. Seifzadeh, T. Grund, and K. Kamacı, "Enhancing corrosion resistance and radiation shielding of AISI 304 SS with Nb and Mo-added $Al_{0.3}$CrFeCoNi-based high-entropy alloy coatings in 3.5 wt. % NaCl: The effect of environmental temperature," J. Alloys Compd. **1020**, 179432 (2025).
[83]S. Han, H. Ma, H. Chen, W. Zou, C. Mo, Z. Fan, and L. Li, "The wear, corrosion and antibacterial behaviors of FeCrNiCuAl_x high-entropy alloy coatings prepared by laser cladding for marine applications," J. Mater. Res. Technol. **35**, 5034–5051 (2025).
[84]Y. Tao, N. Ren, Z. Dong, Q. Ma, and H. Zhang, "Improved high-temperature oxidation resistance and enhancement alloy coatings by Cr doping," J. Alloys Compd. **1026**, 180735 (2025).
[85]D. Zhang, Q. Li, C. Chang, G. Zhang, X. Ma, and R. Sun, "Effects of Mn addition on wear and corrosion resistances of AlCoCrFeNi high-entropy alloy coating sprayed by HVOF," J. Mater. Res. Technol. **34**, 627–638 (2025).
[86]A. D. Pogrebnjak, I. V. Yakushchenko, A. A. Bagdasaryan, O. V. Bondar, R. Krause-Rehberg, G. Abadias, P. Chartier, K. Oyoshi, Y. Takeda, V. M. Beresnev, and O. V. Sobol, "Microstructure, physical and chemical properties of nanostructured (Ti–Hf–Zr–V–Nb)N coatings under different deposition conditions," Mater. Chem. Phys. **147**(3), 1079–1091 (2014).
[87]W. Gao, M. Feng, C. Chen, and G. Lian, "Microstructure evolution, wear resistance and corrosion resistance of $CoCrCu_{0.5}FeNiSi_x$ high-entropy alloy coatings fabricated by laser cladding," J. Mater. Res. Technol. **36**, 5539–5558 (2025).
[88]C. Liu, X. Jiang, H. Sun, T. Liu, Z. Wu, and L. Yang, "Steam oxidation properties of graphene reinforced bioinspired laminated CoCrFeNiMn high-entropy alloy matrix composites at 1000 °C," Mater. Today Commun. **38**, 107962 (2024).
[89]J. Kumar, N. Nayan, R. K. Gupta, M. Ramalingam Munisamy, and K. Biswas, "High entropy alloy: Lab to product prototype," Int. J. Metalcast. **17**(2), 860–873 (2022).
[90]J. Bishop-Moser *et al.*, see https://hdl.handle.net/2027.42/146747 for "Manufacturing High Entropy Alloys Pathway to Industrial Competitiveness."
[91]Y. F. Ye, Q. Wang, J. Lu, C. T. Liu, and Y. Yang, "High-entropy alloy: Challenges and prospects," Mater. Today **19**(6), 1–14 (2016).
[92]F. Madewu, "Strength—Ductility synergy of lightweight high entropy alloys," Eng. Rep. **3**, 1–10 (2025).
[93]T. Xie *et al.*, "An overview of high-throughput synthesis for advanced high-entropy alloys," MGE Adv. **3**, e87 (2025).
[94]K. Kuwabara, H. Shiratori, T. Fujieda, K. Yamanaka, Y. Koizumi, and A. Chiba, "Mechanical and corrosion properties of AlCoCrFeNi high-entropy alloy fabricated with selective electron beam melting," Addit. Manuf. **23**, 264–271 (2018).
[95]Q. Sui, Z. Wang, J. Wang, S. Xu, F. Zhao, L. Gong, B. Liu, J. Liu, and G. Liu, "The microstructure and mechanical properties of the additive manufactured AlCoCrFeNi high entropy alloy," Mater. Sci. Eng. A **833**, 142507 (2022).
[96]S. Arun, N. Radhika, and B. Saleh, *Effect of Additional Alloying Elements on Microstructure and Properties of AlCoCrFeNi High Entropy Alloy System: A Comprehensive Review* (The Korean Institute of Metals and Materials, 2024).
[97]R. J. Vikram, K. Dash, S. K. Aramanda, and S. Suwas, "Design of a nickel–cobalt based eutectic high entropy alloy $(NiCo)_{1.7}$AlCrFe with hierarchical microstructural length scales," Philos. Mag. **103**(16), 1592–1602 (2023).
[98]H. Cheng, H. Luo, C. Fan, X. Wang, and C. Li, "Accelerated design of high-entropy alloy coatings for high corrosion resistance via machine learning," Surf. Coat. Technol. **502**, 131978 (2025).
[99]H. Zhang, X. Shi, F. Xu, Y. Zhang, Y. Liu, L. Shu, and D. Zuo, "Machine learning to explore the corrosion resistance and descriptor-property correlation analysis of high-entropy alloys," Mater. Today Commun. **46**, 2352–4928 (2025).
[100]S. Sivaraman, N. Radhika, and M. Abubaker Khan, "Machine learning-driven prediction of wear rate and phase formation in high entropy alloy coatings for enhanced durability and performance," IEEE Access **13**, 33956–33975 (2025).
[101]X. Tan, W. Trehern, A. Sundar, Y. Wang, S. San, T. Lu, F. Zhou, T. Sun, Y. Zhang, Y. Wen, Z. Liu, M. Gao, and S. Hu, "Machine learning and high-throughput computational guided development of high temperature oxidation-resisting Ni–Co–Cr–Al–Fe based high-entropy alloys," npj Comput. Mater. **11**(1), 1–16 (2025).
[102]R. Chawuthai, T. Promchan, J. Rojsanga, S. Chandra-ambhorn, T. Nilsonthi, P. Wongpromrat, E. Bumrungthaichaichan, and A. Anantpinijwatna, "Novel method for predicting the cracks of oxide scales during high temperature oxidation of metals and alloys by using machine learning," Sci. Rep. **15**(1), 1–15 (2025).
[103]Z. Dong, A. Sun, S. Yang, X. Yu, H. Yuan, Z. Wang, L. Deng, J. Song, D. Wang, and Y. Kang, "Machine learning-assisted discovery of Cr, Al-containing high-entropy alloys for high oxidation resistance," Corros. Sci. **220**, 111222 (2023).
[104]H. C. Ozdemir, A. Nazarahari, B. Yilmaz, D. Canadinc, E. Bedir, R. Yilmaz, U. Unal, and H. J. Maier, "Machine learning—Informed development of high entropy alloys with enhanced corrosion resistance," Electrochim. Acta **476**, 143722 (2024).
[105]S. Srivastava, I. Kumar, M. Kumar, H.G. Shakier, B. Swathi, and N. Chahuan, "Machine learning and artificial intelligence for advanced materials processing: A review on opportunities and challenges," in *E3S Web of Conferences* (EDP Sciences, 2024), p. 505.